

8-2007

NONLINEAR MODELING OF THE ADSORPTION-INDUCED SURFACE STRESS IN PIEZOELECTRICALLY-DRIVEN MICROCANTILEVER BIOSENSORS

Mana Afshari

Clemson University, mafshar@clemson.edu

Follow this and additional works at: https://tigerprints.clemson.edu/all_theses



Part of the [Engineering Mechanics Commons](#)

Recommended Citation

Afshari, Mana, "NONLINEAR MODELING OF THE ADSORPTION-INDUCED SURFACE STRESS IN PIEZOELECTRICALLY-DRIVEN MICROCANTILEVER BIOSENSORS" (2007). *All Theses*. 154.

https://tigerprints.clemson.edu/all_theses/154

This Thesis is brought to you for free and open access by the Theses at TigerPrints. It has been accepted for inclusion in All Theses by an authorized administrator of TigerPrints. For more information, please contact kokeefe@clemson.edu.

NONLINEAR MODELING OF THE ADSORPTION-INDUCED SURFACE
STRESS IN PIEZOELECTRICALLY-DRIVEN MICROCANTILEVER
BIOSENSORS

A Thesis
Presented to
the Graduate School of
Clemson University

In Partial Fulfillment
of the Requirements for the Degree
Master of Science
Mechanical Engineering

by
Mana Afshari
August 2007

Accepted by:
Nader Jalili, Committee Chair
Darren M. Dawson
Mohammed F. Daqaq

ABSTRACT

Microcantilever-based biosensors are rapidly becoming an enabling sensing technology for a variety of label-free biological applications due to their extreme applicability, versatility and low cost. These sensors operate through the adsorption of species on the functionalized surface of microcantilevers. The adsorption of biological species induces surface stress which originates from the molecular interactions such as adhesion forces of attraction/repulsion, electrostatic forces or the surface charge redistribution of the underlying substrate. This surface stress, consequently, alters the resonance frequency of the microcantilever beam.

This study presents a general framework towards modeling resonance frequency changes induced due to the surface stress arising from the adsorption of biological species on the surface of the microcantilever. Very few works have dealt with the effect of surface stress on the resonance frequency shifts of microcantilevers and mainly assume a simple model for the vibrating microcantilever beam. In the proposed modeling framework, the nonlinear terms due to beam's flexural rigidity from macro- to micro-scale as well as varying nature of the adsorption induced surface stress are considered.

It is first shown that the nonlinearity of the system originates from two different sources; namely, microcantilever flexural rigidity and adsorption induced surface stress. All these nonlinearities are formulated into the general equation of motion of the vibrating microcantilever. It is then shown that the dynamic mode of biosensing formulated in the paper is much more sensitive than the static mode to the change in the properties of the adsorbed biological species.

DEDICATION

To my family in Iran and my friends in Clemson

ACKNOWLEDGMENTS

I sincerely thank my advisor, Dr. Nader Jalili for his support and guidance during my Master's studies in every aspect. It was a great chance to work in his research group, which left me with many wonderful qualities. Helpful suggestions from my advisory committee members, Dr. Darren M. Dawson and Dr. Mohammed F. Daqaq, and the financial supports through National Science Foundation under CAREER Grant No. DMI-0238987, are also greatly appreciated.

TABLE OF CONTENTS

	Page
TITLE PAGE	i
ABSTRACT	iii
DEDICATION	v
ACKNOWLEDGEMENTS	vii
LIST OF TABLES	xiii
LIST OF FIGURES	xv
 CHAPTER	
1. INTRODUCTION	1
Research Motivation	1
Thesis Overview	2
 2. MICROCANTILEVER-BASED SENSING	 5
Background and Literature Review	6
Microcantilever-based Sensing Applications	7
Surface Stress Sensing	8
Ultra-small Mass Sensing	12
Temperature Sensing	12
 3. MICROCANTILEVER-BASED BIOSENSING	 13
Different Methods of Biosensing	14
Quartz Crystal Microbalance (QCM)	14
Microcantilever Biosensors' Modes of Detection	17
Static Mode	17
Uniform Curvature Assumption and Modeling the Surface Stress	 20
Static Deflection based on Energy Dissipation	23

Table of Contents (Continued)

	Page
Static Deflection based on the Molecular Interactions.....	24
Dynamic Mode.....	27
Taut-String Model Approximation	27
Beam with Axial Force Model Approximation	28
Utilizing Buckling Analogy in Formulating the Adsorption-induced Shift in Resonance Frequency.....	30
Recent Developments of the Microcantilever Biosensors	31
Sensitivity Enhancement.....	31
Potential and Practical Medical Applications	35
 4. NONLINEAR MODELING OF PIEZOELECTRICALLY-DRIVEN MICROCANTILEVER BIOSENSORS.....	 39
Piezoelectric Actuators	40
Molecular Arrangement of the Adsorbed Biological Species and the Modeling the Adsorption Induced Surface Stress.....	43
Origin of the Adsorption Induced Surface Stress	44
Intermolecular Forces of Attraction and Repulsion.....	45
Lennard-Jones Constants of A and B	47
Electrostatic Forces.....	50
Capillary Forces	51
The General Equation of Motion	
Microcantilever utilizing Hamilton's Principle	52
Potential Energy of the Microcantilever Beam.....	54
Potential Energy due to the Beam's Structure Having the PZT Layer on Its Surface	54
Potential Energy due to the energy storage of PZT Layer.....	56
Potential Energy due to the Adsorbed Biological Layer	58
Total Potential Energy of the Microcantilever Beam with the PZT Layer and the Adsorbed Biological Layer	60
Kinetic Energy of the Microcantilever Beam	60
General Equation of Motion of the Microcantilever Beam	61

Table of Contents (Continued)

	Page
5. SOLUTION TO THE NONLINEAR EQUATIONS OF MOTION.....	71
Numerical Simulations and Results	73
The Effect of the Attached PZT Layer	78
The Effect of Both PZT and the Adsorbed Biological Layers.....	80
6. SENSITIVITY STUDY OF THE STATIC MODE DETECTION	83
A New Approach toward Solution of the Nonlinear Equation of Motion	84
Numerical Simulations and Results	87
Sensitivity of the Static vs. the Dynamic Detection Mode	89
7. CONCLUSIONS AND FUTURE WORK	93
Conclusions.....	93
Future Work and Directions.....	94
APPENDIX: SAMPLE CODES AND BLOCK DIAGRAMS USED FOR NUMERICAL SIMULATIONS AND EXPERIMENTS	97
REFERENCES	103

LIST OF TABLES

Table	Page
4.1 Lattice structure for some elements	49
5.1 Experimental resonance frequencies before (f_1), and after adsorption (f_{ads}), and the variation in microcantilever's resonance frequency (Δ)	75
5.2 Simulation results for constants A and B and the corresponding frequency.....	76
5.3 Simulation results for constants A and B and the corresponding frequencies for PZT-driven microcantilever.....	81

LIST OF FIGURES

Figure	Page
2.1 Schematic behaviour of the adsorbed biological species on the surface of a microcantilever and their molecular interactions	5
2.2 Schematic of the DNA hybridization experiment. Each cantilever is functionalized on one side with a different oligonucleotide base sequence, (a) before the injection and adsorption of the biological species, (b) after the injection of the first complementary oligonucleotide, where the hybridization occurs on the cantilever and deflects it for an amount of Δx	8
2.3 Schematic of a microcantilever biosensor, (a) having only one functionalized surface and studied via the static detection mode, (b) having both surfaces functionalized hence studied via the dynamic detection mode	9
2.4 Schematic of the absorption-induced surface stress sensing	10
2.5 Schematic of the spontaneous adsorption of straight-chain thiol molecules on a gold coated cantilever	11
3.1 Schematic of a cantilever chemical sensor with optical lever readout. Microcantilever surfaces modified with (a) nanobeads, (b) cavitand receptors, and (c) thin polymeric film to improve cantilever response or selectivity. (d) Depiction of a bioaffinity interaction microcantilever	13
3.2 Schematic of the quartz crystal which is the main part of a QCM	15
3.3 Schematic of a commercially available quartz crystal microbalance	16
3.4 Schematic diagram showing loading of free edges of cantilever plate by moments per unit length $M_{app} = \Delta\sigma t / 2$	22

List of Figures (Continued)

Figure	Page
3.5 Schematic of the uniformly distributed surface stress model	23
3.6 Arrangement of atoms (or molecules) on cantilever surface	25
3.7 Position of surface atoms (or molecules) on the deflected microcantilever beam.....	26
3.8 Taut-string approximation of the microcantilever beam	28
3.9 Schematic view of a microcantilever with uniform surface stress.....	29
3.10 Microcantilever with fractional surface stresses coverage	29
3.11 Scheme of microcantilever based DNA detection	35
3.12 Surface of a microcantilever biosensor covered with <i>E. coli</i>	36
3.13 Schematic of mass increase due to bacterial growth on the surface of microcantilever sensor: (a) Freshly adsorbed <i>E. coli</i> cells on the surface of microcantilever, (b) The bacterial cells start to grow	36
3.14 SEM image of <i>Listeria innocua</i> bacteria nonspecifically adsorbed on the surface of a microcantilever	37
3.15 A microcantilever beam utilized for the mass sensing of the adsorbed vaccinia virus particle.....	38
4.1 Schematic of a microcantilever biosensor with the attached biological species and the piezoelectric layer on its surface.....	40
4.2 (a) A stacked design piezoelectric actuator, (b) A laminar design piezoelectric actuator	42
4.3 PZT strip bonded to the surface of a beam	43

List of Figures (Continued)

Figure	Page
4.4 Arrangement of a monolayer of the adsorbed biological species on microcantilever surface before the deflection of the microcantilever beam	44
4.5 Schematic of a fully assembled alkane thiol SAM	44
4.6 The interacting forces between tip and nanoparticles in AFM positioning.....	45
4.7 Arrangement of the adsorbed atoms (molecules) on microcantilever surface	46
4.8 (a) Steady-state cantilever deflections caused by immobilization of ssDNA (sequence K-30) at different PB concentrations, (b) Steady-state changes in cantilever deflection for hybridization of 30-nt-long ssDNA (sequences K-30 and K9-30) at different PB concentrations	51
4.9 Schematic of capillary effect during a sphere and flat surface contact, with e being the initial thickness of the water, h the tip-surface distance, r and ρ the radii of curvature of the meniscus.....	52
4.10 (a) Schematic of the microcantilever with the PZT and the adsorbed biological layers on its surface, (b) Coordinate system of the microcantilever beam	53
4.11 Schematic of a segment of the microcantilever beam and the PZT layer on its surface	55
4.12 Arrangement of a monolayer of biological species on microcantilever surface after the deflection of microcantilever ..	59
5.1 Frequency response of a microcantilever with properties listed in Eq. (5.12) and the adsorbed biological species on its surface having Lennard-Jones constants of $A=1.3 \times 10^{-72} \text{ J.m}^6$ and $B=0.4 \times 10^{-135} \text{ J.m}^{12}$	77

List of Figures (Continued)

Figure	Page
5.2 Linear frequency response of the PZT-driven microcantilever	79
5.3 Nonlinear frequency response of the PZT-driven microcantilever	80
5.4 Nonlinear frequency response of the PZT-driven microcantilever covered by a biological layer with $A=1\times 10^{-72}$ J.m ⁶ and $B=0.4\times 10^{-135}$ J.m ¹²	82
6.1 The static deflection of the microcantilever with length=500 (μm), width= 100 (μm) and thickness=1 (μm)	88
6.2 The static deflection of five microcantilever beams differing only in their lengths	89
6.3 Different static deflections of the PZT-driven microcantilever with the properties listed in Eqs. (6.13) and (6.14) for different Lennard-Jones A constants	90
6.4 Resonance frequencies of the first mode of vibration for the PZT-driven microcantilever with the properties listed in Eqs. (6.13) and (6.14) for different Lennard-Jones A constants.....	91
7.1 Cantisense functionalisation unit	95
7.2 Polytec state-of-the-art micro system analyzer MSA 400	96
A.1 Simulink® block diagram of deriving the frequency response of the vibrating microcantilever beam	97

CHAPTER 1

INTRODUCTION

Research Motivation

Microcantilever-based biosensors are rapidly becoming an enabling sensing technology for a variety of label-free biological applications due to their extreme applicability, versatility and low cost. These sensors operate through the adsorption of species on the functionalized surface of microcantilevers.

Very few works have dealt with modeling the effect of surface stress on the resonance frequency shifts of microcantilevers and mainly assume a simple model for the vibrating microcantilever beam. Studying “macro-scale” cantilever beams, these simple models provide relatively good representation of the physical systems. For the case of microcantilevers, however, the molecular forces are no longer negligible and must be taken into account in modeling the surface stress.

Thesis Overview

This thesis presents a general framework towards modeling resonance frequency changes induced due to the surface stress arising from the adsorption of biological species on the surface of the piezoelectrically-driven microcantilever.

The molecular interactions of the adsorbed biological species which induce the surface stress are explained in Chapter 4 and the attraction/repulsion forces are considered in the potential energy formulation.

Utilizing the Hamilton's principle, the general equation of motion of the resonating microcantilever is also formulated in Chapter 4. In the proposed modeling framework derived in Chapter 4, the nonlinear terms due to beam's flexural rigidity from macro- to micro-scale as well as varying nature of the adsorption induced surface stress are considered. It is first shown that the nonlinearity of the system originates from two different sources; namely, microcantilever flexural rigidity and adsorption induced surface stress.

Through numerical simulation given in Chapter 5, it is demonstrated that the nonlinearity due to the surface stress does not have a considerable effect on the resonance frequency change of the microcantilever. However, nonlinearity due to flexural rigidity (which is directly attributed to beam's dimensions) plays an important role in the resonance frequency shift, and hence, in the resultant molecular recognition capability.

A new method of formulating the adsorption induced surface stress as a function of the static deflection of the microcantilever is given in Chapter 6. Most of the previous works in this area are based on the Stoney's simple equation. In the proposed method, the molecular interactions of the adsorbed biological species are modeled based on the Lennard-Jones attraction/repulsion potential. As a result, the sensitivity of the static detection mode (based on the proposed

method) is compared to that of the dynamic mode. It is shown that the dynamic mode of biosensing is much more sensitive to the change in the properties of the adsorbed biological species, when compared to conventional static mode detection mechanism.

CHAPTER 2

MICROCANTILEVER-BASED SENSING

Recently, microfabricated silicon cantilevers for atomic force microscopy (AFM) have been used to measure changes in the surface stress of solids or the added mass to their surface. These experiments lead to the idea of making extremely sensitive sensor platform for chemical and biological detections, as schematically depicted in Figure 2.1.

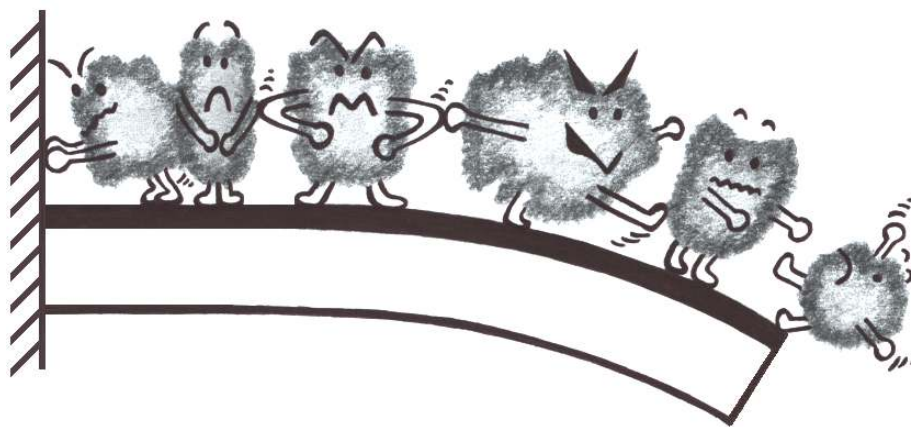


Figure 2.1: Schematic behaviour of the adsorbed biological species on the surface of a microcantilever and their molecular interactions

Background and Literature Review

The idea of applying macroscopic cantilevers goes back to about a century ago, when Stoney utilized cantilevers' deflection for measuring the deposition induced surface stress of beams in an electrochemical environment [59] and Galileo performed cantilevers as platforms for investigating the strength of materials [44]. In late 70's, Taylor *et al.* utilized cantilevered beam sensors for the detection of gasses [62].

Microcantilevers were first used in Scanning Force Microscopy (SFM). These microcantilevers deflect due to the interaction forces between their tip and the sample. It was observed that temperature variations and adsorption of vapors cause parasitic cantilever deflection in SFM [66]. Although this parasitic deflection was undesirable for the SFM, it triggered the idea of applying microcantilevers as chemical and temperature sensors. Thundat *et al.* showed that the resonance frequency variation of SFM cantilevers can be used for measuring the amount of loaded mass of the adsorbed water and mercury vapors [66].

Simultaneously, Gimzewski *et al.* used micromachined cantilevers as temperature and heat flow sensors and as calorimeters for measuring the heat generated by chemical reactions [4, 5, 22]. It is important to note that in 1993 (prior to Thundat *et al.* and Gimzewski *et al.*'s investigations) Cleveland *et al.* utilized microcantilevers' sensing potential for precisely calculating the spring constant of the SFM microcantilevers. Their nondestructive method included the addition of small masses at the end of the microcantilevers and measuring the

resulting shift in resonance frequency of the beam [14]. Although they established a unique calibration method for SFM microcantilevers, they did not pay attention to the unrevealed sensing potential of microcantilevers and missed the opportunity of being the pioneers in the field of microcantilever sensing. Cleveland *et al.*'s method was later modified due to its low accuracy resulting from the practical difficulties and errors of placing the added mass at a specific position on the microcantilevers [52].

From the observations of Thundat *et al.* in Oak Ridge National Laboratory and Gimzewski *et al.* in IBM Zurich Research Laboratory and Cambridge University, a new era was established in sensor technology. Microcantilever sensors attracted a lot of attention due to their simplicity, extremely small size and potential for extremely high sensitivity.

Microcantilever-based Sensing Applications

In the beginning, microcantilevers were mainly utilized as chemical [36, 49, 63, 65, 68], thermal [10, 13, 17, 36, 46, 48] and physical [44, 45, 69] sensors. These sensors were generally considered to perform in air or in vacuum, resulting in the ignorance of environmental damping effect on the resonance frequency of microcantilevers. Utilizing microcantilever sensors for studying biological systems under native conditions and investigating processes at liquid-solid interface brought the idea of considering the damping effect of the surrounding

media on the resonance frequency of microcantilevers [70]. It was not until 1996, when the applicability and potential of microcantilevers as biosensors attracted attention [6, 7, 9].

Surface Stress Sensing

What makes microcantilevers the useful platform for chemical and biological sensing is the functionalization of one or both sides of these microcantilevers. This means that for biosensing, for example, if only one surface shows high affinity to the targeted species and the other surface is relatively passivated, these targeted species will be adsorbed to one side of the microcantilever, and as a result, the adsorption induced surface stress bends the microcantilever, as schematically depicted in Figure 2.2.

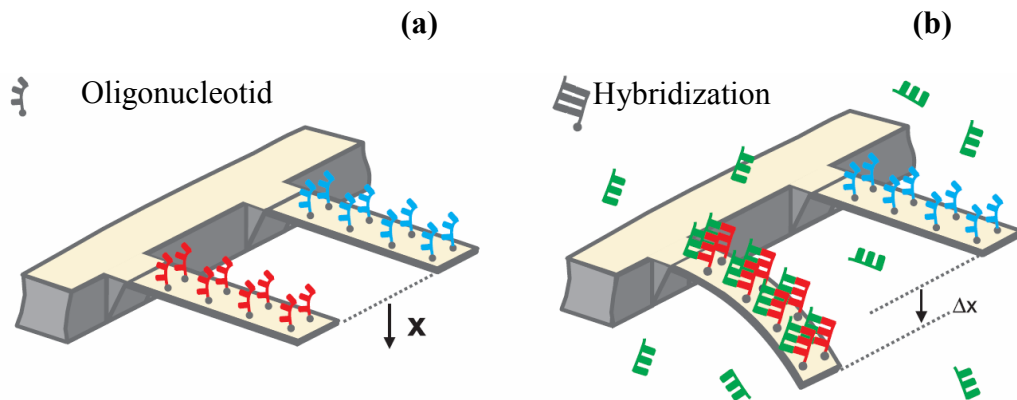


Figure 2.2: Schematic of the DNA hybridization experiment. Each cantilever is functionalized on one side with a different oligonucleotide base sequence, (a) before the injection and adsorption of the biological species, (b) after the injection of the first complementary oligonucleotide, where the hybridization occurs on the cantilever and deflects it a distance of Δx [20]

If only one side of the microcantilever is functionalized, as depicted in Figure 2.3 (a), the adsorption induced surface stress may be formulated by either measuring the deflection or the shift in the resonance frequency of the microcantilever. However, if both sides of the microcantilever are functionalized, as depicted in Figure 2.3 (b), the static deflection measurement will not be a practical method for surface stress measurement. Hence, the measurements of the shift in the resonance frequency of the microcantilevers should be utilized for the adsorption-induced surface stress measurements.

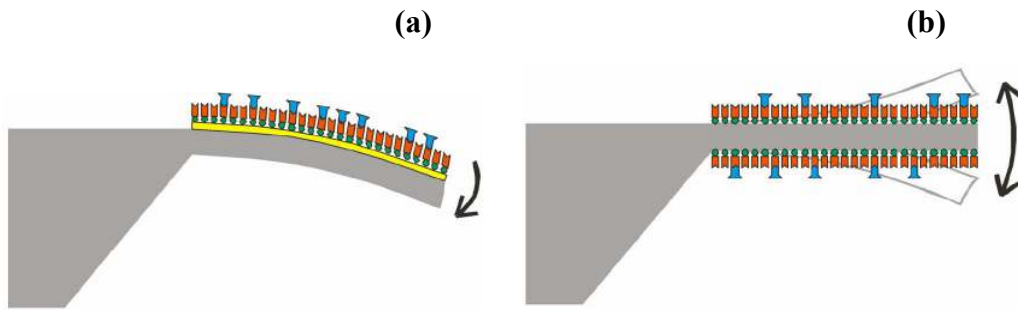


Figure 2.3: Schematic of a microcantilever biosensor, (a) having only one functionalized surface and studied via the static detection mode, (b) having both surfaces functionalized hence studied via the dynamic detection mode [31]

There exist two different types of surface stress sensors:

1) Those sensors measuring the *adsorption*-induced surface stress; target molecules are being adsorbed on to the functionalized surface of the sensor. This type of sensors will be extensively studied in the following chapters.

2) Those sensors measuring the *absorption*-induced surface stress; target molecules will penetrate into the sensing layer which has been deposited on the surface of the sensor, which will result in the swelling of the sensing layer. A schematic of this type of sensing is depicted in Figure 2.4.

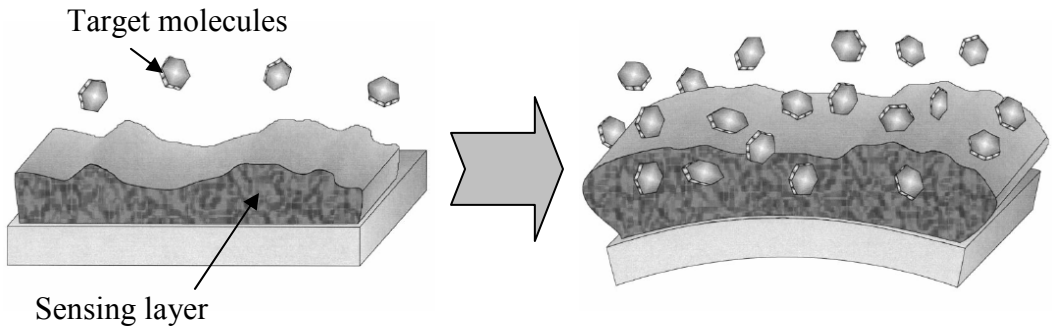


Figure 2.4: Schematic of the absorption-induced surface stress sensing [37]

Surface Stress Definition

Surface stress is a macroscopic quantity that is governed by microscopic processes. The surface stress may be defined in various ways, depending on the particular framework being investigated [49].

In general, changes in the surface stress is mainly due to the changes in Gibbs free energy associated with the adsorption process, as all binding reactions are driven by the reduction of free energy [36]. Surfaces usually tend to expand as a result of the adsorptive processes, as schematically depicted in Figure 2.5.

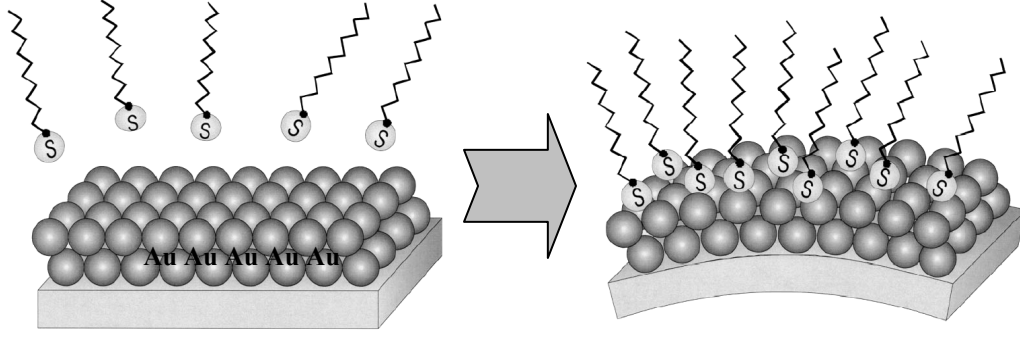


Figure 2.5: Schematic of the spontaneous adsorption of straight-chain thiol molecules on a gold coated cantilever [63]

Using the first law of thermodynamic and differential calculus, Shuttleworth formulated an equation relating the surface stress σ and surface free energy γ as follows [13],

$$\sigma = \gamma + A \frac{\partial \gamma}{\partial A} \quad (2.1)$$

where A is the surface area and the ratio of $\frac{dA}{A}$ is the surface strain ($\partial \varepsilon$). In many cases, the contribution from the surface strain term can be neglected and the free energy change is approximately equal to the change in the surface stress [63].

A more general formulation of the Shuttleworth is the one with the stress defined as a tensor, as follows [13],

$$\sigma_{ij} = \gamma \delta_{ij} + \frac{\partial \gamma}{\partial \varepsilon_{ij}}, \quad i, j = 1, 2, 3 \quad (2.2)$$

where δ_{ij} is the Kronecker delta and ε_{ij} is the elastic strain tensor.

Ultra-small Mass Sensing

The natural frequency of free vibration of a mechanical flexible system depends on the system parameters; typically its mass, spring constant, modulus of elasticity, dimensions, etc. Variations in system parameters change the natural frequency. When the target molecules are adsorbed on to the functionalized surface of the microcantilever sensor, its mass changes, therefore, the natural frequency is altered by a small but detectable amount. This forms the basis of the dynamic mode of operation for the microcantilever sensor. The matter particle can be a biological or chemical agent.

Temperature Sensing

AFM cantilevers can be used as precise thermometers or calorimeters by exploiting the bimetallic effect [10, 36]. If the cantilever beam is coated by a material having a different coefficient of thermal expansion than that of the material making up the cantilever itself, it will undergo a deflection as a result of temperature changes.

CHAPTER 3

MICROCANTILEVER-BASED BIOSENSING

In recent years, micro and nano-mechanical oscillators have been used as a new class of biological sensors. Such cantilever sensors are successfully applied in the fields of genomics and proteomics. The main advantage of these types of biosensors compared to other biosensing methods is the ability to detect different types of biological species by only altering the functionalized surface of the microcantilever sensors, as schematically depicted in Figure 3.1.

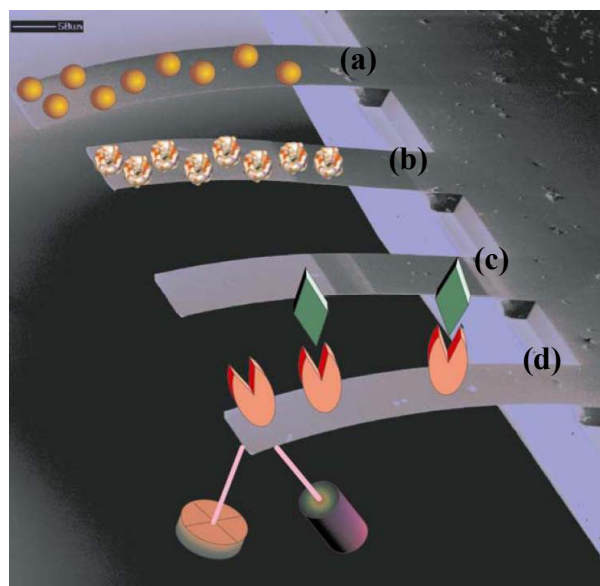


Figure 3.1: Schematic of a cantilever chemical sensor with optical lever readout. Microcantilever surfaces modified with (a) nanobeads, (b) cavitand receptors, and (c) thin polymeric film to improve cantilever response or selectivity. (d) Depiction of a bioaffinity interaction microcantilever [55]

Different Methods of Biosensing

Before microcantilevers were found to be useful biosensing platforms, the most common bio-detection method was achieved through adding fluorescent tags to the targeted molecules [1]. However, microcantilever biosensors turned out to be better bio-detection tools as the molecular recognition is directly and specifically transduced into nanomechanical responses in a cantilever array. Hence, there is no need for labeling targeted molecules with fluorescence or radioactive tags. Moreover, by utilizing microcantilevers as biosensors, various application fields differ only in the functional layer on the cantilever interface.

Quartz crystal microbalance (QCM) is another biosensor which works under similar working principles as the microcantilever biosensors. An overview of this type of bio-detection system and its disadvantages are explained in the following subsection.

Quartz Crystal Microbalance (QCM)

The microgravimetric QCM is a promising candidate for biosensor applications, and its potential for the detection of DNA hybridization has been demonstrated recently. Although the QCM has a high inherent sensitivity (capable of measuring sub-nanogram levels of mass changes), methods for improving the detection limit of this device are being sought to enable wide application of the technique for DNA hybridization detection [75].

QCM has been used for a long time to monitor thin film deposition in vacuum or gas. It consists of a thin quartz disc sandwiched between a pair of electrodes, as depicted in Figure 3.2. Utilizing the piezoelectric properties of quartz, the crystal is excited to oscillation by applying an AC voltage across its electrodes [77].

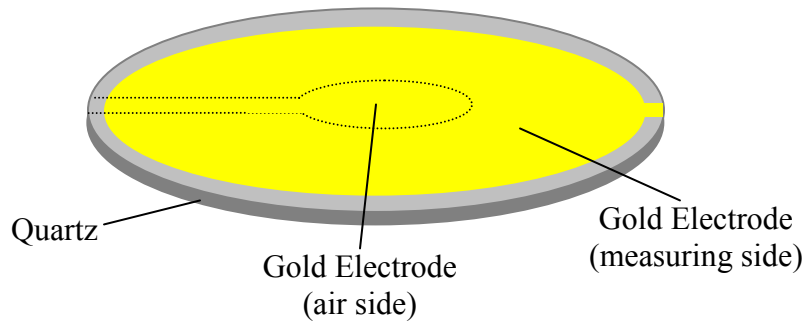


Figure 3.2: Schematic of the quartz crystal which is the main part of a QCM [76]

The resonance frequency (f) of the crystal depends on the total adsorbed oscillating mass. When a thin film is attached to the crystal surface, the resonance frequency of the oscillating crystal decreases. If the film is thin and rigid the decrease in frequency is proportional to the mass of the film. In this way, the QCM operates as a very sensitive platform [77]. Schematic of a commercially available QCM is depicted in Figure 3.3.

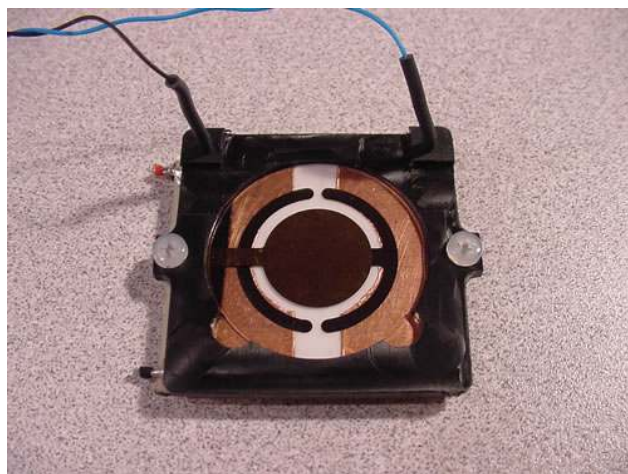


Figure 3.3: Schematic of a commercially available quartz crystal microbalance [78]

Microcantilever resonance-based DNA detection method is analogous to QCM in the vibration-working mode. However, there are several major differences between the two, as explained below.

- 1) QCM sensor element is more than 100 times bigger than the microcantilever sensors and requires large amount of target molecules to give out a detectable signal.
- 2) The microcantilever enables the construction of high-density sensor array to detect multiple species simultaneously at high efficiency. QCM is difficult to be integrated for its relative complex structure and means of detection.
- 3) Most importantly, parallel detection of multiple species at the same time can be made possible by depositing different functionalization layer on the microcantilever surfaces.

Microcantilever Biosensors Modes of Detection

A microcantilever biosensor can be operated in the following two different modes:

Static mode: In this mode, the deflection of the microcantilever beam is measured. Having the deflection of the beam after the adsorption of biological species, adsorption induced surface stress can be accordingly calculated.

Dynamic mode: In this mode, the shift in resonance frequency of the beam is measured. Knowing the shift of resonance frequency after the adsorption, the adsorption induced surface stress and/or the added mass can be calculated.

Various mathematical models have been developed to explain the two modes of microcantilever operation. Some of them are described in the following subsections.

Static Mode

Long before the first microfabricated cantilevers were created, changes in surface stresses of these systems had been studied by measuring minute deformations of relatively thin (up to 1 mm) plates, referred to as the “beam-bending” technique. Koch and Abermann demonstrated that the bending of a cantilever can be measured with sufficient sensitivity that the change in the stress due to the deposition of a single monolayer on one side can be detected [34].

This technique was first proposed by Stoney in 1909 to measure the residual stresses in metallic thin films deposited by electrolysis [59]. In this method, the surface stress is calculated from the observed deformation of the rectangular plate using the following simple equation, which is commonly referred to as Stoney's formula:

$$z = \frac{3(1-\nu)L^2}{t^2 E} \sigma \quad (3.1)$$

where z is the displacement of the cantilever, ν , L , t and E are the Poisson's ratio, length, thickness and modulus of elasticity of the cantilever, respectively, and σ is the adsorption-induced differential surface stress.

The Stoney's formula is applicable to thin plates with uniform thickness exhibiting small deflections, where the effect of in-plane loading on the transverse (out-of-plane) deflections is negligible.

Corrections to the Stoney's Formula

In the “thin-film approximation” considered in Stoney's formula, that is, in the case of a thin film (coating) on a thick substrate, the average stress or macrostress acting in the coating (σ_c) can be expressed in a very simple manner as [32]

$$\sigma_c \cong E'_c \Delta \varepsilon_0 \quad (3.2)$$

where E'_c is the biaxial modulus of the coating ($E' = \frac{E}{1-\nu}$) and $\Delta\varepsilon_0$ characterizes the strain mismatch between coating and the substrate ($\Delta\varepsilon_0 = \varepsilon_{c,0} - \varepsilon_{s,0}$). However, in order to extend the Stoney's formula to the case of “thick” films, the general theory of elastic interactions in multilayer laminates [67] must be used instead of Eq. (3.2), which can be best expressed as [33]

$$\sigma_c(z) = E'_c \left[\frac{E'_s t_s}{E'_s t_s + E'_c t_c} \Delta\varepsilon_0 + \left(\frac{t_s + t_c}{2} - \theta - z \right) K \right] \quad (3.3)$$

where z is measured from the bottom surface of the substrate, K is the curvature, t_s and t_c are the thickness of substrate and coating, respectively, and the parameter θ is defined as follows

$$\theta = \frac{t_s t_c (E'_s - E'_c)}{2(E'_s t_s + E'_c t_c)} \quad (3.4)$$

By defining parameters $\gamma_1 = \frac{E'_c}{E'_s}$ and $\delta = \frac{t_c}{t_s}$, the ratio of the corrected average stress intensity in the coating ($\bar{\sigma}_c$) to that calculated by Stoney's formula (σ_{st}) is simply found to be [32]

$$\frac{\bar{\sigma}_c}{\sigma_{st}} = \frac{1 + \gamma_1 \delta^3}{1 + \delta} \quad (3.5)$$

which emphasizes that, in fact, it is a straightforward matter to extend Stoney's equation to situations involving thick coatings.

Based on Eq. (3.5), it is shown that Stoney's original formula does not cause serious errors for thickness ratios of $\delta \leq 0.1$, but fails to properly describe the variation of stress with thickness and cannot be relied upon for thickness ratios of $\delta > 0.1$ [32]. In the absence of information on the biaxial modulus of the coating, Atkinson's approximation can be applied [3]. It considers a correction factor equal to $\frac{1}{1+\delta}$ for the Stoney's formula, resulting in $\sigma_{At} = \frac{\sigma_{st}}{1+\delta}$. Atkinson's approximation yields much better results (compared to Stoney's formula) and can be used for thickness ratios up to about 40%.

Uniform Curvature Assumption and Modeling the Surface Stress

The original Stoney's equation assumes that surface stress is uniformly changed during the deflection and relates the surface stress to the radius of curvature of the cantilever, R , as [64]

$$\frac{1}{R} = \frac{6(1-\nu)}{Et^2} \sigma \quad (3.6)$$

This formula assumes a uniform curvature for the whole deflected structure which is quite extreme for the nonlinear analysis of film large deflection and its limitation is illustrated in [32] and [19].

The uniform curvature assumption is identical to modeling the cantilever under the surface stress as an unrestrained (free) plate, which violates the clamp

boundary condition of the “cantilever” at $x=0$. In other words, the Stoney’s equation describes the surface stress-induced deformation of a cantilever plate only if; 1) the length of the plate greatly exceeds its width, and 2) the point under consideration is far from the clamp. Another characteristic of the Stoney’s formula in the modeling of the problem is to replace the adsorption-induced surface stress as a moment applied at the structure’s free end. Considering both these assumptions and their shortcomings, Sader has improved the plate’s modeling by replacing the differential surface stress $\Delta\sigma$ applied to the faces of the plate by moments per unit length of magnitude $\Delta\sigma t/2$ loaded at the free edges of the plate, as depicted in Figure 3.4, where t is the thickness of the plate [51]. The clamped end boundary condition is also considered in Sader’s formulation. Since an exact analytical solution for a cantilever plate is extremely difficult, if not impossible to obtain, finite element method is utilized to obtain a qualitative overview of the cantilever plate’s behavior. An approximate analytical formula is also derived to replace the Stoney’s formula in situations where it is found to be inaccurate.

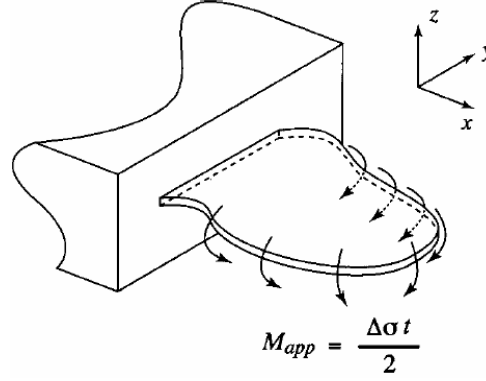


Figure 3.4: Schematic diagram showing loading of free edges of cantilever plate by moments per unit length $M_{app} = \Delta\sigma t / 2$ [51]

In order to improve the modeling of the cantilever, the adsorption-induced surface stress can be replaced by a moment (similar to Stoney's and Sader's formulation) together with a concentrated transverse load applied at the free end of the cantilever [43]

None of these analyses that model the surface stress as a moment (or moment together with force) applied at the structure's free edge or free end, take the influence of the surface stress on structure stiffness into account. This may be improved by modeling the applied surface stress as an area stress which is uniformly distributed on the upper surface of the beam, as depicted in Figure 3.5 [13, 74]. Applying the principle of virtual work, the equation of motion of the beam and the boundary conditions can then be derived. Utilizing this modeling, it is demonstrated how the stiffening effect of tensile stress becomes important when the magnitude of the surface stress becomes relatively large [74].

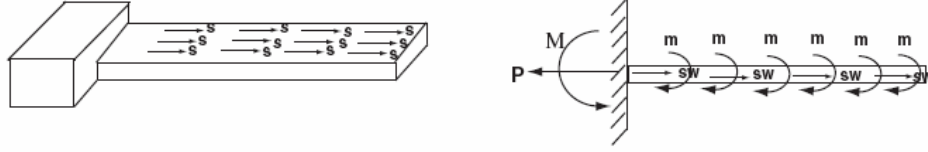


Figure 3.5: Schematic of the uniformly distributed surface stress model [74]

Static Deflection based on Energy Dissipation

It is well established that molecular adsorption changes the surface free energy of a substrate surface due to the fact that all binding reactions are driven by the reduction of free energy, as mentioned in Chapter 2. The Shuttleworth equation was also given in Eq. (2.1) relating the surface stress and the surface free energy, as rewritten below,

$$\sigma = \gamma + A \frac{\partial \gamma}{\partial A} \quad (3.7)$$

However, the Shuttleworth equation is somewhat difficult to apply to Stoney's formula (or any of its modified versions) since the second term in Eq. (3.7) (i.e. $\frac{\partial \gamma}{\partial A}$) depends on beam curvature, which is an unknown. Hence, both the Stoney and Shuttleworth equations must be solved simultaneously to obtain σ and z (the deflection of the microcantilever beam). Ibach has carefully studied the surface stress on crystalline cantilevers induced by adsorption of single atoms [27]. However, when dealing with complex molecules like proteins, as it is often

the case in biochemical sensing, there are several other possible sources of stress rather than simple ion adsorption onto a clean crystal surface.

Electrostatic interaction between neighboring adsorbed species, changes in surface hydro-phobicity, and conformational changes of the adsorbed molecules can all induce stresses which may contrast with each other and make the change in stress not directly related to the receptor-ligand binding energy or the rupture force. As an example, it has been recently observed how adsorption of complementary single-stranded DNA onto the cantilever surface can induce either compressive or tensile stress depending on the ionic strength of the buffer in which the hybridization takes place [75]. This behavior is interpreted as the interplay between two opposite driving forces; reduction of the configurational entropy of the adsorbed DNA after hybridization which tends to lower the compressive stress, and intermolecular electrostatic repulsion between adsorbed DNA which tends to increase the compressive stress.

Static Deflection based on the Molecular Interactions

In modeling the surface stress, there exists a method which is based on the energy potential in the first layer of atoms attached to one surface of a microcantilever and the elastic potential energy in the microcantilever itself [16]. The energy potential in the adsorbed layer is formulated based on the molecular interactions of the adsorbed species. The assumption that the first atomic layer on

the beams surface plays a dominate role in microcantilever deflections is supported by the experimental works of Martinez *et al.* [41] and Schell-Sorokin *et al.* [54] who measured changes in curvature in cantilevered-thin plates due to adsorption of submonolayer of different atoms in ultrahigh vacuum conditions. Regarding this assumption, the arrangement of adsorbed atoms (or molecules) on the surface of microcantilever is modeled as shown in Figure 3.6.

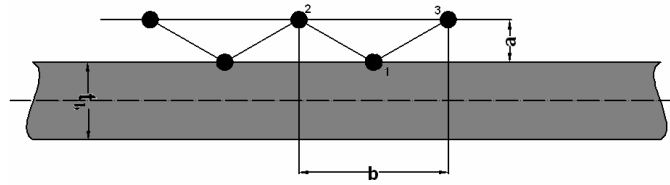


Figure 3.6: Arrangement of atoms (or molecules) on cantilever surface

According to the proposed model, atoms in the attached film are attracted and repulsed according to the Lennard–Jones potential formula

$$w(r) = \frac{-A}{r^6} + \frac{B}{r^{12}} \quad (3.8)$$

where r is the spacing between atoms (molecules) and A and B are Lennard–Jones constants. Part of this potential is transferred into the cantilever as elastic strain energy causing the beam to deflect. The equilibrium configuration of the cantilever is determined by minimizing the total potential function, which is made up of the Lennard–Jones potential and the elastic energy in the cantilever. By considering a simple model of the curved beam (after the bending of the

microcantilever) as depicted in Figure 3.7, the total atomic and elastic bending potential energy is found to be

$$U = U_s + U_b = \frac{-A}{(b-z)^6} + \frac{B}{(b-z)^{12}} + 2 \left\{ \frac{-A}{[1/4(b-z)^2 + a^2]^3} + \frac{B}{[1/4(b-z)^2 + a^2]^6} \right\} + \frac{1}{2} EI \left(\frac{1}{R} \right)^2 b \quad (3.9)$$

where R is the radius of curvature and a and b are parameters shown in Figures 3.6 and 3.7.

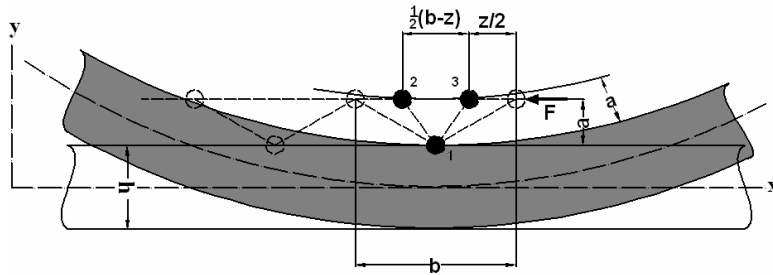


Figure 3.7: Position of surface atoms (or molecules) on the deflected microcantilever beam [16]

In order to find the radius of curvature of the deflected beam, and hence the deflection of the beam, the amount of U in Eq. (3.9) must be a relative minimum, which is determined from [16]

$$\frac{dU}{d\left(\frac{c}{R}\right)} = 0 \quad (3.10)$$

Remark: Instead of the Lennard-Jones formula used in deriving U_s , the simpler van der Waals potential [Eq. (3.11)] may be used

$$U_s = -\frac{C}{r^6} \quad (3.11)$$

where the interaction constant C can be determined as $C = 1.05 \times 10^{-76} cd \text{ (Jm}^6\text{)}$, where c and d are van der Waals constants depending on the type of atoms (molecules) [16].

Dynamic Mode

Contrary to static mode, there exist different models for analyzing the effect of the adsorption induced surface stress on the resonance frequency shift of the microcantilever. Some of these models are explained in the following subsections.

Taut-String Model Approximation

This model approximates the microcantilever beam as a taut string and models the effect of surface stress as a constant force along the string, as depicted in Figure 3.8.

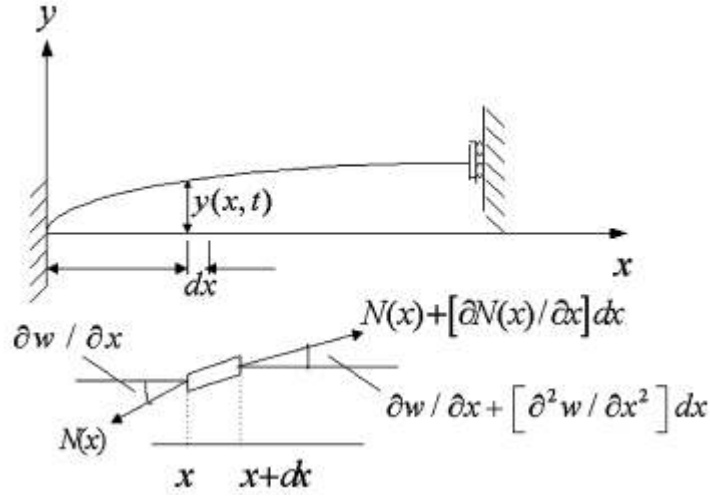


Figure 3.8: Taut-string approximation of the microcantilever beam [50]

The equation of motion of the beam can be represented as [50]

$$N v'' + \rho A_b \ddot{v} = 0 \quad (3.12)$$

where $N = \sigma L$ is the longitudinal force and $v(s, t)$ is the vertical displacement of the microcantilever. Prime denotes derivative with respect to position s and the over dot indicates derivative with respect to time t .

Beam with Axial Force Model Approximation

In the simplest model, surface stress is expressed as non-varying force (F) and moment applied at the free end of the microcantilever, as depicted in Figure 3.9.

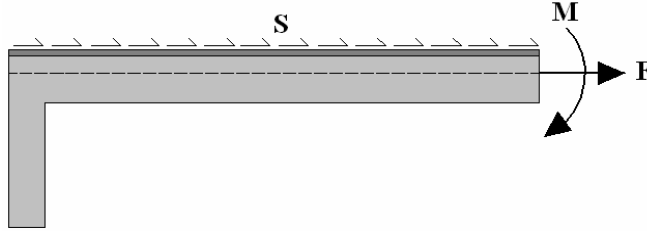


Figure 3.9: Schematic view of a microcantilever with uniform surface stress

Having this force, the equation of motion of the microcantilever beam can be expressed as [39]

$$EI v'''' - Fv'' + \rho A_b \ddot{v} = 0 \quad (3.13)$$

This model was later modified by assuming that the axial force due to surface stress varies along the microcantilever and the surface stress exists only on a fraction of the microcantilever as depicted in Figure 3.10.

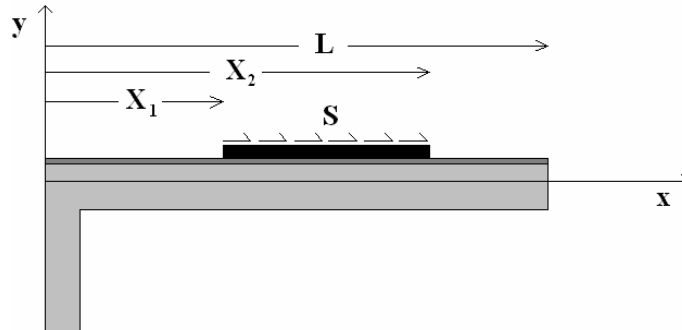


Figure 3.10: Microcantilever with fractional surface stresses coverage

This assumption modifies the equation of motion of the beam as follows [50]

$$EI v'''' - (F(s)v')' + \rho A_b \ddot{v} = 0 \quad (3.14)$$

where

$$F(s) = \sigma L f(s), \text{ with } f(s) = \begin{cases} \frac{s_2}{L} - \frac{s_1}{L} & 0 < s < s_1 \\ \frac{s_2}{L} - \frac{s}{L} & s_1 < s < s_2 \end{cases} \quad (3.15)$$

Studying “macro-scale” cantilever beams, both of these models provide relatively good representation of the physical systems. For the case of microcantilevers, however, the molecular forces are no longer negligible and must be taken into account in modeling the surface stress, as detailed in the next chapter.

Utilizing Buckling Analogy in Formulating the Adsorption-induced Shift in Resonance Frequency

The effect of adsorption induced surface stress on the change of the microcantilever resonance frequency has been found considering the buckling-resonance analogy as [42]

$$f_{ads} = \frac{1}{2\pi\sqrt{3}} \left[1 + \frac{2\sigma L^3}{EI\pi^2} \right]^{1/2} \left(\frac{\alpha_i}{L} \right)^2 \sqrt{\frac{EI}{\rho A_b}} \quad (3.16)$$

where ρ and A_b are the mass density and cross-sectional area of the microcantilever, respectively, and α_i is the i -th positive root of the eigenfrequency equation

$$\cos \alpha_i \cosh \alpha_i + 1 = 0 \quad (3.17)$$

As the resonance frequency of the microcantilever beam can be easily found from the general equation of motion of the vibrating beam, the main effort has been done in formulating the surface stress (and its effects) into the equation of motion of the microcantilever.

Recent Developments in Microcantilever Biosensors

Sensitivity Enhancement

Physical dimensions play an important role in the sensitivity of microcantilever sensors for mass detection. Modeling the microcantilever as a simple 1D oscillator, its natural frequency may be formulated as follows [13]

$$f = \frac{1}{2\pi} \sqrt{\frac{K}{m_b}} \quad (3.18)$$

where K is the spring constant and $m_b = n m_{beam}$ is the effective beam mass with m_{beam} being its actual mass and n being a geometric parameter accounting for

the non point-mass distribution. n has a typical value of 0.24 for a rectangular microcantilever beam.

Presence of mass on the microcantilever surface results in the generation of differential surface stress. This changes the spring constant, which in turn changes the natural frequency. In general, the altered resonance frequency can be formulated as follows [13]

$$f_{\delta} = \frac{1}{2\pi} \sqrt{\frac{K + \delta K}{m_b + n\delta m}} \quad (3.19)$$

where δK is the change in the spring constant attributed to adsorption induced surface stress and δm being the added mass.

It has been shown that if adsorption is localized (i.e., end loading), the change in resonance frequency due to change in spring constant can be neglected. If the spring constant K can be formulated as follows [64]

$$K = \frac{Eb h^3}{4L^3} \quad (3.20)$$

with E being the Young's modulus of elasticity for the microcantilever beam material and b , h , and L being width, thickness and length of the beam, respectively. Then, the resonance frequency f of the microcantilever beam can be given as follows [64]

$$f = \frac{h}{2\pi(0.98)L^2} \sqrt{\frac{E}{\rho}} = \frac{1}{2\pi} \sqrt{\frac{K}{m_{eq}}} \quad (3.21)$$

where m_{eq} is the equivalent mass consisting of mass of microcantilever beam and adsorbed mass. If m_d is the mass added at the end of the microcantilever beam, then $m_{eq} = nm_d + m_b$.

The shifted resonance frequency f_δ can be given by [64]

$$f_\delta = \frac{1}{2\pi} \sqrt{\frac{Ebh^3}{4nL^3(m_d + \rho bhL)}} \quad (3.22)$$

The adsorbed mass δm can then be determined from the change in the resonance frequency using the following equation [64]

$$\frac{f^2 - f_\delta^2}{f^2} = \frac{\delta m}{m} \quad (3.23)$$

The mass sensitivity S_m of the sensor can be given by [64]

$$S_m = \lim_{\Delta m \rightarrow 0} \frac{1}{f} \frac{\Delta f}{\Delta m} = \frac{1}{f} \frac{df}{dm}, \quad \Delta m = \frac{\delta m}{A_s} \quad (3.24)$$

where A_s is the active area of the sensor. The sensitivity is the fractional change in resonant frequency with addition of mass to the sensor. When applied to the microcantilever sensor, the sensitivity can be expressed as follows [64]

$$\begin{aligned}
S_m &= \frac{1}{\rho h} \quad \text{for distributed load} \\
&= \frac{-\zeta_1}{2\rho(\zeta_1 h_d + 0.24h)} \quad \text{for end load}
\end{aligned} \tag{3.25}$$

where ζ_1 and h_d are the fractional area coverage and thickness of the deposited mass at the end loaded microcantilever beam. The minimum detectable mass Δm_{\min} can be given by the following equation [64]

$$\Delta m_{\min} = \frac{1}{S_m} \frac{\Delta f_{\min}}{f} \tag{3.26}$$

Reduction in dimensions can lead to improvement in sensitivity of resonance mode of the mass sensors. However, size reduction leads to different sensor fabrication difficulties. Several different methods have been explored to improve sensitivity without having to reduce the microcantilever dimensions further. One of the most recent one of these presents a method of increasing the sensitivity by using a frequency tuning approach to measure mass changes. The method uses a closed loop strategy to measure mass change in parametric resonance based sensor. A DC offset is applied to the sensor as a feedback signal to compensate for the frequency shift at the boundary of the parametric resonance region. Mass changes are detected by measuring the DC offset feedback [73].

Potential and Practical Medical Applications

Microcantilever biosensors are useful platforms for different medical diagnostics. They have been successfully used in DNA detection [23, 60, 71]. The sensing or detection of DNA strands is important in the fabrication of DNA probe arrays useful in DNA sequencing or gene mapping applications [23]. A schematic of microcantilever-based DNA detection is depicted in Figure 3.11.

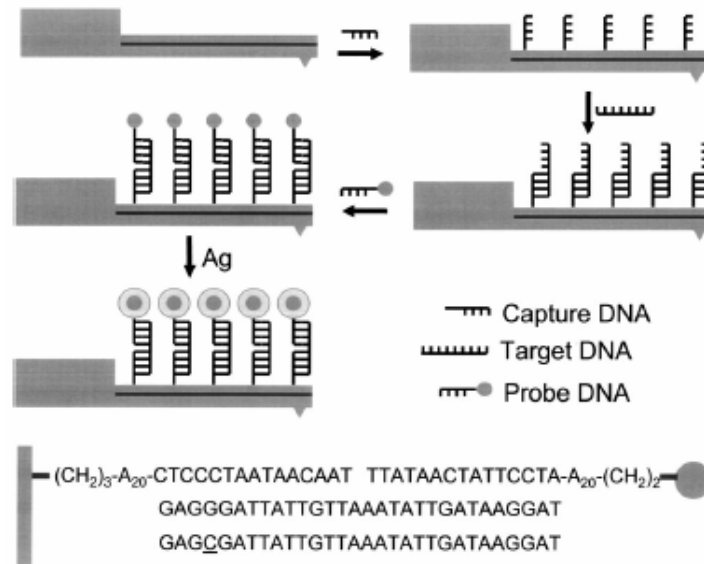


Figure 3.11: Scheme of microcantilever based DNA detection [60]

The ability to quickly identify the presence of specific DNA components may also be important in the rapid identification of certain bio-terror agents [23].

Bacterial infections are common and involved in many forms of disease, such as food poisoning. Rapid detection of bacteria may lead to the fast

adjustment of antibiotic treatment, which in turn leads to decreased mortality and lowers the hospitalization cost [21].

One of the most common bacteria used in the experiments is *Escherichia coli* (referred to as *E. coli*). Surfaces of the microcantilevers are covered with this type of bacteria, as depicted in Figure 3.12. A schematic of the growth of the adsorbed *E. coli* on the surface of the microcantilever is also depicted in Figure 3.13.

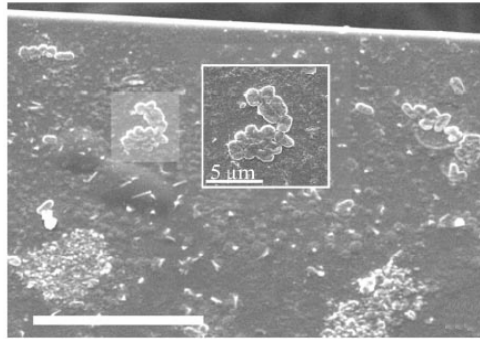


Figure 3.12: Surface of a microcantilever biosensor covered with *E. coli* [21]

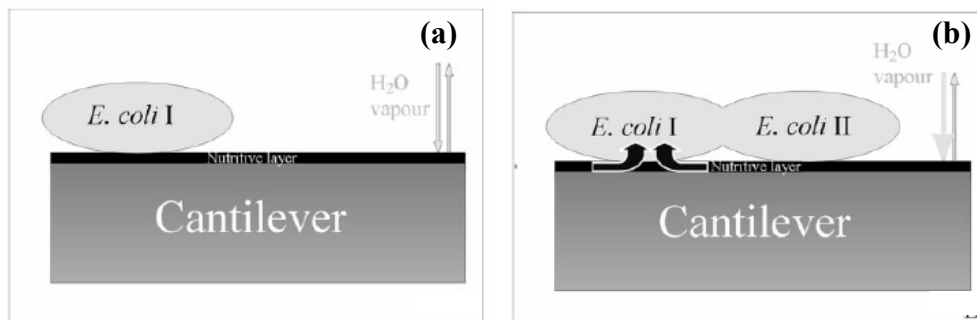


Figure 3.13: Schematic of mass increase due to bacterial growth on the surface of microcantilever sensor: (a) Freshly adsorbed *E. coli* cells on the surface of microcantilever, (b) The bacterial cells start to grow [21]

Another type of bacteria used in the experiments is *Listeria innocua*. In this case, the surface of the microcantilever is covered with affinity-purified polyclonal antibody for *Listeria innocua* [24]. An image of a microcantilever covered with *Listeria innocua* bacteria is depicted in Figure 3.14.

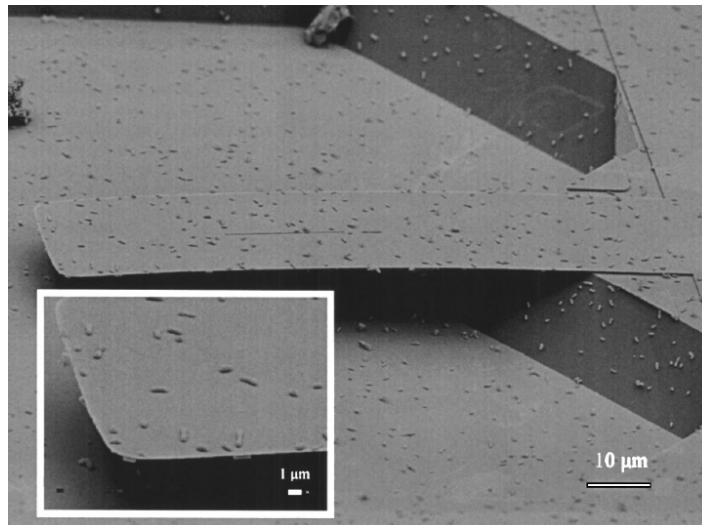


Figure 3.14: SEM image of *Listeria innocua* bacteria nonspecifically adsorbed on the surface of a microcantilever [24]

Different virus particles such as baculovirus and single virus particle may also be detected utilizing microcantilever biosensors [25, 29]. Figure 3.15 depicts a microcantilever with the attached vaccinia virus particle on its surface.

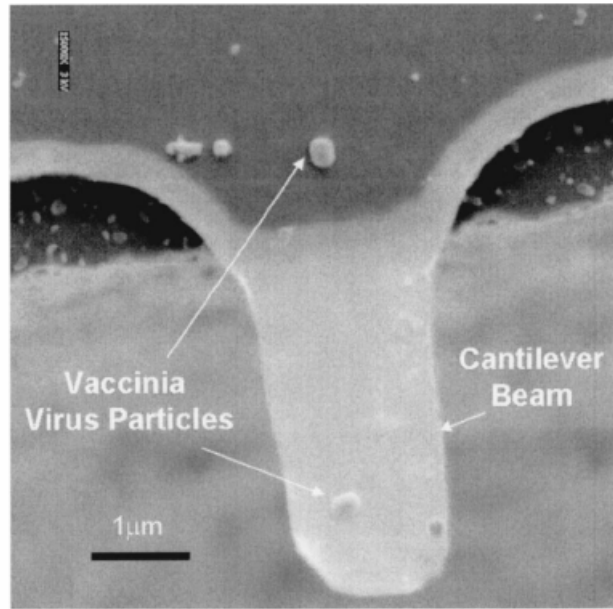


Figure 3.15: A microcantilever beam utilized for the mass sensing of the adsorbed vaccinia virus particle [25]

Microcantilever biosensors may also be utilized in detection of protein [38, 53], glucose [61] and thiol molecules [28].

CHAPTER 4

NONLINEAR MODELING OF PIEZOELECTRICALLY-DRIVEN MICRO-CANTILEVER BIOSENSORS

As explained in the previous chapters, microcantilevers are useful platforms for biosensing applications. In this chapter, formulating the adsorption-induced surface stress into the equation of motion of the vibrating microcantilever is of interest. As the microcantilever beam is being operated in the dynamic mode of detection, appropriate actuation and frequency read-out systems are required. Here, it is assumed that the microcantilever beam is actuated via the applied voltage to the piezoelectric layer attached on its surface. This PZT layer may cover all (as depicted in Figure 4.1) or part of the microcantilever surface.

Having the surface of the microcantilever functionalized, target biological species will specifically adsorb to the surface of the microcantilever and they will form a biological layer on microcantilever surface, as depicted in Figure 4.1.

In order to derive the equation of motion of the vibrating microcantilever beam and formulate the adsorption-induced surface stress, the potential energy of the attached PZT layer and the adsorbed biological layer is needed. Hence, an overview of the piezoelectric actuators and the nature of the molecular interactions of the adsorbed biological species are given in the beginning of this chapter.

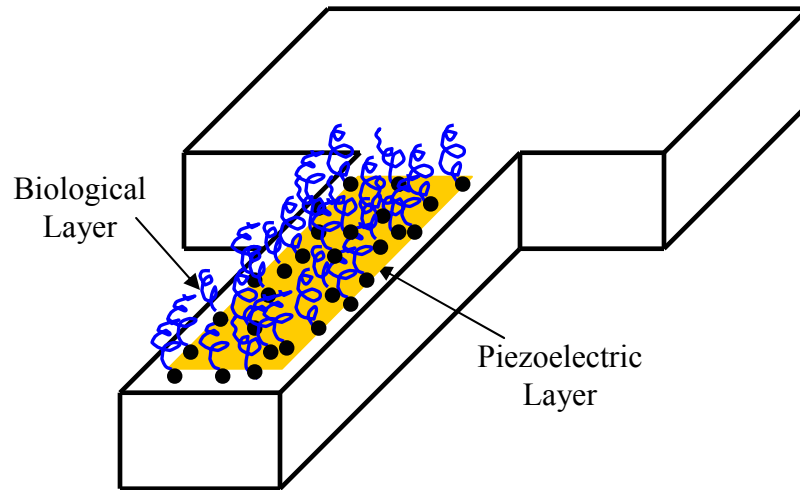


Figure 4.1: Schematic of a microcantilever biosensor with the attached biological species and the piezoelectric layer on its surface

Piezoelectric Actuators

The piezoelectric effect was discovered in 1880 [2]. The ability of certain crystalline materials (ceramics) to generate an electrical charge in proportion of an externally applied force is called *direct* piezoelectric field. This direct effect is used in force transducers. According to the *inverse* piezoelectric effect, an electric field parallel to the direction of polarization induces an expansion of the ceramic. The direction of expansion with respect to the direction of the electrical field depends on the constants appearing in the constitutive equations. The material can be manufactured in such a way that one of the coefficients dominates the others. One of the materials most frequently used for piezoelectric actuators is lead-zirconium-titanate, or PZT [2]. From here on, PZT is used to refer to the piezoelectric actuator unless otherwise stated.

For the inverse piezoelectric effect, the electrical and mechanical constitutive equations are coupled as follows [2]:

$$S = s^E T + dE \quad (4.1)$$

where constant d (with the dimension of C/N or m/V) relates the strain to the electric field E (with the dimension of V/m) in the absence of mechanical stress and s^E (having dimension of m²/N) refers to the compliance when the electric field is constant. S and T are the strain and stress vectors with dimensions of (m/m) and (N/m²), respectively.

There exist two basic types of piezoelectric actuators: the stacked design or linear actuators and the laminar design or the spatially distributed actuators, as depicted in Figure 4.2.

Here, utilizing the laminar design piezoelectric actuators is of interest and they will be considered in deriving the equations of motion through out the following modelings.

In the laminar design, thin piezoelectric films are bonded on the structure, as depicted in Figure 4.3, where the PZT strip is attached to the surface of the beam. In this case, the geometrical arrangement is such that the piezoelectric coefficient d_{31} dominates the design and the useful direction of expansion is normal to that of the electric field [2] Considering the beam and PZT layer depicted in Figure 4.3, and assuming that the thickness of the PZT layer is small

compared to that of the beam, the following stress relation within the PZT layer may be formulated [2],

$$\sigma_{11} = E_p \varepsilon_{11} - E_p d_{31} \frac{P(t)}{h_p} \quad (4.2)$$

where $\frac{P(t)}{h_p}$ is the electric field generated by controlling the voltage $P(t)$ applied to the electrodes.

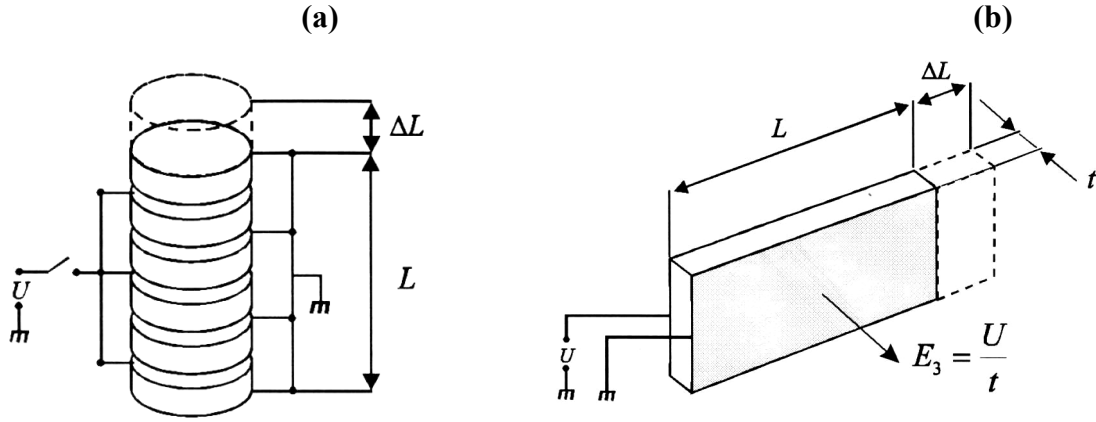


Figure 4.2: (a) A stacked design piezoelectric actuator, (b) A laminar design piezoelectric actuator [2]

Now that the stress generated within the PZT layer is formulated according to Eq. (4.2), the equation of motion of the PZT-actuated microcantilever beam may be formulated utilizing the Hamilton's principle method, as described in the following sections.

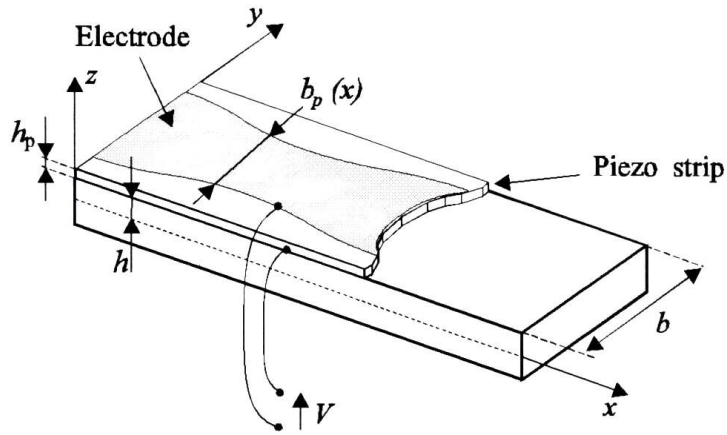


Figure 4.3: PZT strip bonded to the surface of a beam [2]

Molecular Arrangement of the Adsorbed Biological Species and the Modeling the Adsorption Induced Surface Stress

In case of chemical microcantilever sensors, experiments show that only the first atomic layer on the microcantilever surface plays a dominant role in the amount of induced surface stress [47, 54]. In regard to this assumption, the simplest model for the arrangement of the adsorbed species is as depicted in Figure 4.4. However, this molecular arrangement is best for the chemical species (such as Mercury) and may not be useful for the adsorption of the biological species. Biological species (e.g., Thiol molecules, protein or DNA) do not have such structured arrangements as depicted in Figure 4.4. As an example, self assembled monolayers (SAM) of Thiol molecules are assumed to be arranged as depicted in Figure 4.5. For simplicity, it is assumed in the present work that the

arrangement of the adsorbed biological species is similar to that depicted in Figure 4.4.

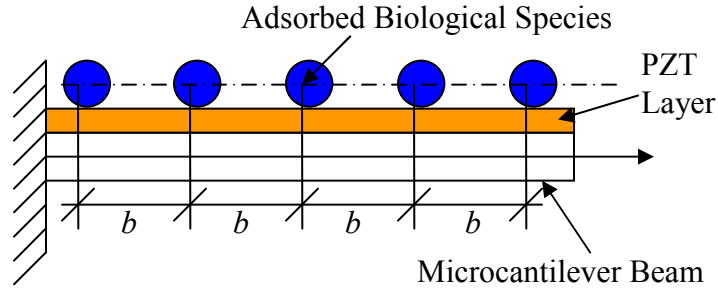


Figure 4.4: Arrangement of a monolayer of the adsorbed biological species on microcantilever surface before the deflection of the microcantilever beam

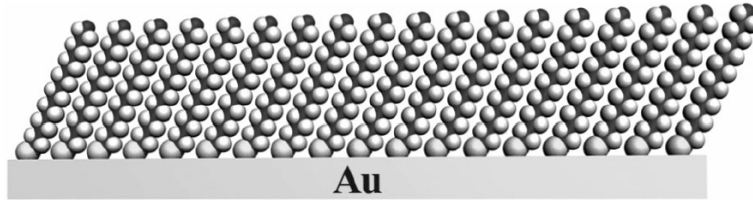


Figure 4.5: Schematic of a fully assembled alkane thiol SAM [28]

Origin of the Adsorption Induced Surface Stress

Molecules of the adsorbed biological species on the surface of microcantilever apply intermolecular adhesion forces to their neighboring molecules. In AFM, when the tip comes to contact with the sample particles, there will be different forces applied to tip and particle as depicted in Figure 4.6.

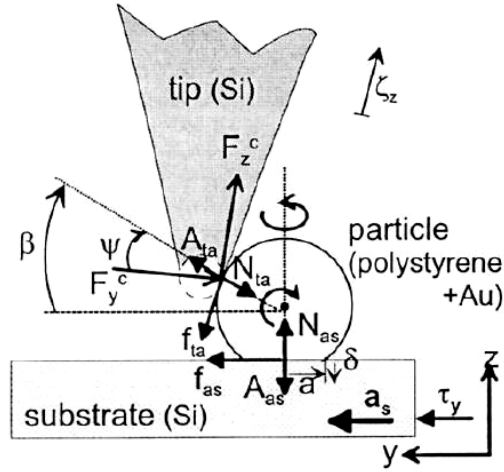


Figure 4.6: The interacting forces between tip and nanoparticles in AFM positioning [57]

Repulsive contact forces, A_{as} and A_{ta} are the adhesion forces. The main components of these adhesion forces are van der Waals, capillary, and electrostatic forces [57].

In microcantilever sensing method, the only forces present are adhesion ones. In this section, the presence of different types of adhesion forces in biosensing microcantilevers are verified, and tried to be formulated.

Intermolecular Forces of Attraction and Repulsion

Considering the chemical microcantilever sensors, the arrangement of the first layer of the adsorbed species (e.g., mercury) may be simply modeled as depicted in Figure 4.7.

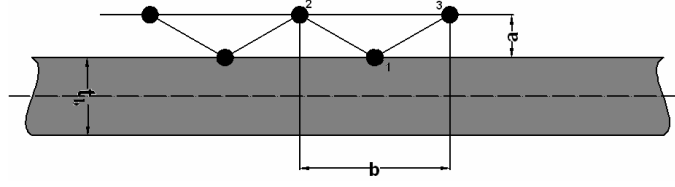


Figure 4.7: Arrangement of the adsorbed atoms (molecules) on microcantilever surface

According to this model, the attraction and/or repulsion forces among atoms (molecules) may be formulated considering the following two approaches:

1) van der Waals Potential Formulation: In some cases, the interactive forces between the adsorbed atoms (molecules) in the monolayer of the biological species may be defined by the van der Waals force of attraction, with its potential is given by the following equation [16],

$$U_s = -\frac{C_{vdw}}{r^6} \quad (4.3)$$

where the interaction constant, C_{vdw} , can be determined from Eq. (4.4) [66],

$$C_{vdw} = 1.05 \times 10^{-76} ed \text{ (J.m}^6\text{)} \quad (4.4)$$

where e and d are van der Waals constants depending on the type of atoms.

2) Lennard–Jones Potential Formulation: This theory is better compared to the van der Waals, since it considers both attraction and repulsion effects. Its potential energy of repulsion and attraction is formulated as follows [16],

$$w(r) = \frac{-A}{r^6} + \frac{B}{r^{12}} \quad (4.5)$$

where r is the spacing between atoms (molecules) and A and B are the Lennard–Jones constants depending on the types of molecules. These constants are available for individual atoms and simple molecules. However, it is not an easy and straight forward procedure to obtain the Lennard-Jones constants for complex molecules and biological species such as protein.

Lennard-Jones Constants of A and B

In case of having two atoms, the Lennard-Jones constants of attraction/repulsion is found to be as $A=10^{-77}\text{Jm}^6$ and $B=10^{-134}\text{Jm}^{12}$. However, in general, in order to find the Lennard-Jones constants, we should follow the steps described bellow:

In general, the Lennard-Jones potential is formulated using the following equation [72],

$$w(r) = 4\varepsilon \left[\left(\frac{\sigma}{r} \right)^{12} - \left(\frac{\sigma}{r} \right)^6 \right] \quad (4.6)$$

where ε is a parameter determining the depth of the potential well and σ is a length scale parameter that determines the position of the potential minimum and is defined as follows [72],

$$\sigma = 2^{-1/6} r_N \quad (4.7)$$

in which r_N is the nearest neighboring distance in the atomic structure. For FCC (face-centered cubic), BCC (body-centered cubic) and diamond crystal structures, r_N equals $a\sqrt{2}/2$, $a\sqrt{3}/2$, and $a\sqrt{3}/4$ respectively, where a is the lattice constant of the specific crystal. The value for parameter a is given in Table 4.1 for some elements.

where z_0 is the equilibrium distance between the two contact planes

$$(z_0 = \left(\frac{2}{15}\right)^{1/6} \sigma) [72].$$

Once σ is known, $\Delta\gamma$ (the work done to move two surfaces from equilibrium separation z_0 to infinity) could be readily obtained from tabulated handbook values or from measurement. Thus, the second parameter of the interatomic Lennard–Jones potential, ε , could be obtained from the following equation [72]:

$$\Delta\gamma = \frac{A_1}{16\pi z_0} \quad (4.8)$$

where

$$A_1 = 4\varepsilon\pi^2 \rho_1 \rho_2 \sigma^6 \quad (4.9)$$

with ρ_1 and ρ_2 being the number density of the atoms of the two bodies.

Table 4.1: Lattice structure for some elements [58]

Element	Structure	a (Å)	σ (Å)	z_0 (Å)
C	Diamond	3.57	1.38	0.98
Na	BCC	4.22	3.26	2.33
Al	FCC	4.05	2.55	1.82
Si	Diamond	5.43	2.09	1.49
K	BCC	5.23	4.03	2.88
Ca	FCC	5.58	3.52	2.52
Fe	BCC	2.87	2.21	1.58
Cu	FCC	3.61	2.27	1.62
Ge	Diamond	5.69	2.20	1.57
Ag	FCC	4.09	2.58	1.84
Au	FCC	4.08	2.57	1.84

In the present work, the simple equation of Eq. (4.5) will be used in formulating the Lennard-Jones potential energy and constants A and B are found by applying an inverse engineering approach on the available results of the related experiments. This will be extensively described in Chapter 5.

Electrostatic Forces

In the experiments held by G. Wu *et al.* [71], V-shaped gold-coated silicon nitride (Au_ySiN_x) microcantilevers are utilized to detect single-stranded DNA (ssDNA). In all stages of the experiments, a solution of sodium phosphate buffer (PB) at $\text{pH} \approx 7.0$ (always with the same pH but possibly different ion concentrations for different experiments) is used to equilibrate the cantilever. Experimental results show that the cantilever deflections for both steps of immobilization and hybridization of ssDNA probe and target were influenced by PB concentration, as depicted in Figure 4.8.

This change in microcantilever deflection induced by change in PB concentration suggests that electrostatic repulsive forces between neighboring DNA molecules must play a role in cantilever motion.

These electrostatic repulsive forces can be reduced by grounding the (semi)-conducting substrate such as Si, Au, or HOPG. However, a model for the electrostatic forces is still desirable for general cases.

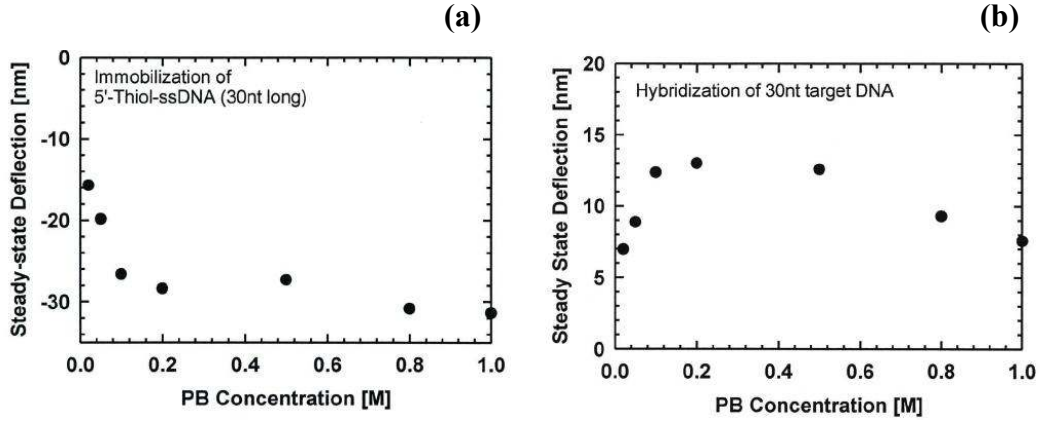


Figure 4.8: (a) Steady-state cantilever deflections caused by immobilization of ssDNA (sequence K-30) at different PB concentrations, (b) Steady-state changes in cantilever deflection for hybridization of 30-nt-long ssDNA (sequences K-30 and K9-30) at different PB concentrations [71]

Capillary Forces

Capillary forces of the model given in Figure 4.6 result from the water layer on the surfaces of the probe and particle. A liquid bridge occurs between the tip and surface at close contact as depicted in Figure 4.9.

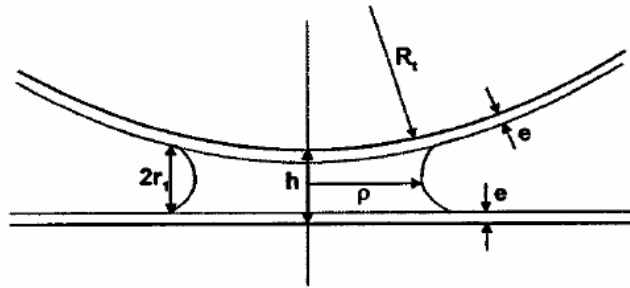


Figure 4.9: Schematic of capillary effect during a sphere and flat surface contact, with e being the initial thickness of the water, h the tip-surface distance, r and ρ the radii of curvature of the meniscus [57]

In microcantilever biosensors, we do not have such contact mode as in AFM applications. Therefore, the capillary effects and forces are neglected in the microcantilever modeling.

The General Equation of Motion Microcantilever utilizing Hamilton's Principle

The PZT-actuated microcantilever biosensor with the adsorbed biological species on its surface utilized in the present modeling framework is depicted in Figure 4.4. Here, the PZT layer and the adsorbed biological layer only cover parts of the microcantilever. However, later in running the simulations it will be assumed, for simplicity, that these two layers cover the whole surface of the microcantilever.

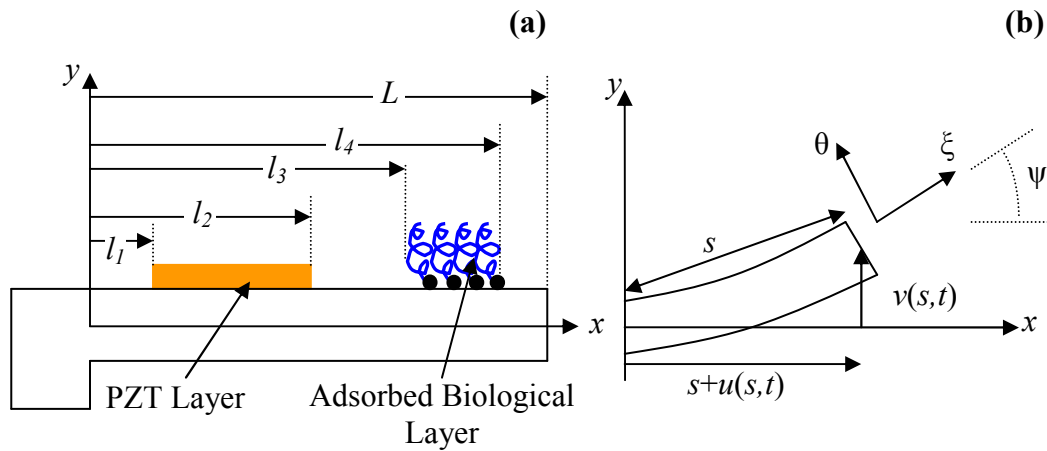


Figure 4.10: (a) Schematic of the microcantilever with the PZT and the adsorbed biological layers on its surface, and (b) coordinate system of the microcantilever beam

The angle ψ is formulated, according to the system depicted in Figure 4.10 (b), as follows,

$$\tan \psi = \frac{v'}{1+u'} \quad (4.10)$$

The curvature (ψ') and the angular velocity ($\dot{\psi}$) of the segment of the beam depicted in Figure 4.10 may then be formulated as follow,

$$\psi' = \frac{v''(1+u') - v'u''}{(1+u')^2 + v'^2} \quad (4.11)$$

$$\dot{\psi} = \frac{\dot{v}'(1+u') - v'\dot{u}'}{(1+u')^2 + v'^2} \quad (4.12)$$

Eqs. (4.11) and (4.12) may be simplified by utilizing Taylor series expansion, assuming $u = O(\epsilon^2)$ and considering only terms of order up to $O(\epsilon^3)$, as follows,

$$\psi' = v'' - v''u' - v'u'' - v''v'^2 \quad (4.13)$$

$$\dot{\psi} = \dot{v}' - \dot{v}'u' - v'\dot{u}' - \dot{v}'v'^2 \quad (4.14)$$

It is known that the beam is inextensible, hence, the following equations apply to the element of the beam depicted in Figure 4.10 [18],

$$f_1(u, v) = 1 - (1+u')^2 - v'^2 = 0 \quad (4.15)$$

Applying Taylor series expansion to Eq. (4.15), u' and v' may be related as follows,

$$u' = \sqrt{1 - v'^2} - 1 \approx -\frac{1}{2}v'^2 + \dots \quad (4.16)$$

Potential Energy of the Microcantilever Beam

The total kinetic energy of the system depicted in Figure 4.10 (a) is only a function of the microcantilever structure. The adsorbed biological layer does not have any effect on the kinetic energy as we have assumed that the effect of adsorbed mass is negligible compared to that of the induced surface stress. However, in formulating the total potential energy, the effects of both PZT and biological layer need to be taken into account. Both kinetic and potential energies of the microcantilever depicted in Figure 4.10 (a) are derived in the following sections.

Potential Energy due to the Beam's Structure Having the PZT Layer on Its Surface

In this section, it is assumed that the PZT layer on the surface of the microcantilever beam doesn't store energy. Hence, its effect will be considered in altering the flexural rigidity of the microcantilever beam only. It is also assumed

that the adsorbed biological layer thickness is much smaller than that of the beam and PZT layer; hence, it doesn't affect the beam's overall flexural rigidity.

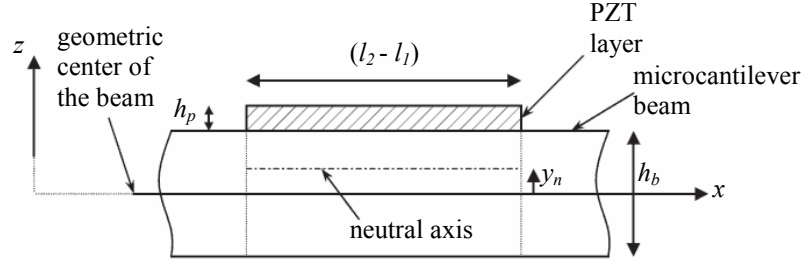


Figure 4.11: Schematic of a segment of the microcantilever beam and the PZT layer on its surface [15]

The overall flexural rigidity of the microcantilever beam and the PZT layer attached on its surface may be formulated considering Figure 4.11, as follows [8],

$$EI(s) = \frac{E_b}{1-\nu_b^2} I_b(s) + \frac{E_p}{1-\nu_p^2} I_p(s) \quad (4.17)$$

where $I_b(s)$ and $I_p(s)$ are formulated using the parallel theorem as follows,

$$I_b(s) = \frac{w_b h_b^3}{12} + (H_{l_1} - H_{l_2}) w_b h_b y_n^2 \quad (4.20)$$

$$I_p(s) = (H_{l_1} - H_{l_2}) \left[\frac{w_p h_p^3}{12} + w_p h_p \left(\frac{h_p}{2} + \frac{h_b}{2} - y_n \right)^2 \right] \quad (4.21)$$

H is the Heaviside function and defined as follows,

$$H_i = \begin{cases} 0 & ; s < i \\ 1 & ; s \geq i \end{cases} \quad (4.18)$$

and y_n , is defined as follows,

$$y_n = \frac{E_p h_p (h_p + h_b)}{2(E_p h_p + E_b h_b)} \quad (4.19)$$

Remark: For a microcantilever beam, the thickness of the beam is typically much smaller than its width and length, thus it is in a “plane strain” configuration. For this reason, the modulus of elasticity of the microcantilever and the PZT layer utilized in Eq. (4.17) is corrected from E to $\frac{E}{1-\nu^2}$ where ν is the Poisson’s ratio of the microcantilever or the PZT layer.

Considering terms of order up to $O(\epsilon^4)$, the potential energy due to the beam’s structure and the attached PZT layer may be formulated as follows,

$$U_{bp} = \frac{1}{2} \int_0^L EI(s) \psi'^2 ds = \frac{1}{2} \int_0^L EI(s) (\nu''^2 - 2\nu''^2 \nu'^2 - 2\nu''^2 u' - 2\nu' \nu'' u'') ds \quad (4.22)$$

Potential Energy due to the Energy Storage of the PZT Layer

The potential energy may be found using the following equation [40],

$$U = \frac{1}{2} \int_0^L M_c \psi' ds \quad (4.23)$$

where M_c is the conservative moment. Considering the second term in Eq. (4.2), which is related to the energy storage of the PZT layer, M_c may be formulated for the PZT layer as follows,

$$\begin{aligned}
 M_c &= \int \sigma_{11} y dA = - \left(H_{l_1} - H_{l_2} \right) \frac{E_p}{1 - \nu_p^2} d_{31} \frac{P(t)}{h_p} \int_{\left(\frac{h_b}{2} - y_n \right)}^{\left(\frac{h_p}{2} + \frac{h_b}{2} - y_n \right)} y dy \\
 &= - \left(H_{l_1} - H_{l_2} \right) \frac{E_p}{1 - \nu_p^2} d_{31} \left(\frac{h_p}{2} + \frac{h_b}{2} - y_n \right) P(t)
 \end{aligned} \tag{4.24}$$

The potential energy due to the energy storage of the PZT layer may then be found by substituting Eqs. (4.13) and (4.23) into Eq. (4.24), as follows,

$$\begin{aligned}
 U_{PZT} &= \frac{1}{2} \int_0^L \left[- \left(H_{l_1} - H_{l_2} \right) \frac{E_p}{1 - \nu_p^2} d_{31} \left(\frac{h_p}{2} + \frac{h_b}{2} - y_n \right) P(t) \right] \left(v'' - v'' u' - v' u'' - v'' v'^2 \right) ds \\
 &= - \frac{1}{2} \int_0^L C_c(s) \left(v'' - v'' u' - v' u'' - v'' v'^2 \right) P(t) ds
 \end{aligned} \tag{4.25}$$

where

$$C_c(s) = \left(H_{l_1} - H_{l_2} \right) \frac{E_p}{1 - \nu_p^2} d_{31} \left(\frac{h_p}{2} + \frac{h_b}{2} - y_n \right) \tag{4.26}$$

Potential Energy due to the Adsorbed Biological Layer

As mentioned before, it is assumed that a monolayer of the biological species is adsorbed on microcantilever surface, where the spacing between the neighboring molecules is b , as depicted in Figure 4.4. This spacing depends on the concentration of the solution of biological species and is not a property of the adsorbed molecules. This spacing changes to $b(1+u')$ and bv' in horizontal and vertical directions, respectively, after the deflection of the microcantilever, as depicted in Figure 4.12.

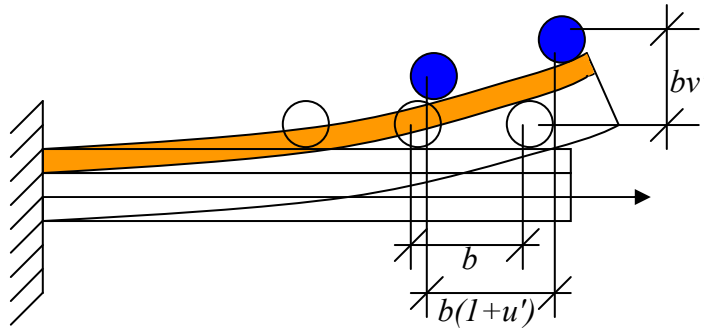


Figure 4.12: Arrangement of a monolayer of biological species on microcantilever surface after the deflection of microcantilever

Applying the Lennard-Jones potential formula to the molecular arrangement of Figure 4.12, the potential energy of the surface stress (originating from the molecular interactions of the neighboring adsorbed biological species) may be found as follows,

$$U_{ss} = 2 \int_0^L \left\{ (H_{l_3} - H_{l_4}) \left[\frac{-A}{b^6 \left[(1+u')^2 + v'^2 \right]^3} + \frac{B}{b^{12} \left[(1+u')^2 + v'^2 \right]^6} \right] \frac{1}{b(1+u')} \right\} ds \quad (4.27)$$

Applying Taylor's series expansion to Eq. (4.27), it will be reduced as follows,

$$U_{ss} = 2 \int_0^L \left(A_1(s) - A_2(s)v'^2 + A_3(s)v'^2u' - A_4(s)u' \right) ds \quad (4.28)$$

where

$$A_1(s) = (H_{l_3} - H_{l_4}) \left(-\frac{A}{b^7} + \frac{B}{b^{13}} \right) \quad (4.29)$$

$$A_2(s) = (H_{l_3} - H_{l_4}) \left(-\frac{3A}{b^7} + \frac{6B}{b^{13}} \right) \quad (4.30)$$

$$A_3(s) = (H_{l_3} - H_{l_4}) \left(-\frac{27A}{b^7} + \frac{90B}{b^{13}} \right) \quad (4.31)$$

$$A_4(s) = (H_{l_3} - H_{l_4}) \left(-\frac{7A}{b^7} + \frac{13B}{b^{13}} \right) \quad (4.32)$$

Total Potential Energy of the Microcantilever Beam with the PZT Layer and the Adsorbed Biological Layer

Putting Eqs. (4.22), (4.25) and (4.28) together, total potential energy of the system can be formulated as follows,

$$\begin{aligned}
 U = U_{bp} + U_{PZT} + U_{ss} = \frac{1}{2} \int_0^L \{ & EI(s) (v''^2 - 2v''^2 v'^2 - 2v''^2 u' - 2v' v'' u'') \\
 & - C_c(s) (v'' - v'' u' - v' u'' - v'' v'^2) P(t) \\
 & + 4 [A_1(s) - A_2(s) v'^2 + A_3(s) v'^2 u' - A_4(s) u'] \} ds
 \end{aligned} \quad (4.33)$$

Kinetic Energy of the Microcantilever Beam

The total kinetic energy of the microcantilever beam and the PZT layer and adsorbed biological layer, as depicted in Figure 4.10 (a), may be formulated as follows,

$$T = \frac{1}{2} \int_0^L [m(s) (\dot{u}^2 + \dot{v}^2)] ds \quad (4.34)$$

where

$$m(s) = w_b \left(\rho_b h_b + (H_{l_1} - H_{l_2}) \rho_p h_p \right) \quad (4.35)$$

It is assumed that the mass of the adsorbed biological layer is negligible.

General Equation of Motion of the Microcantilever Depicted in Figure 4.10 (a)

Having Eqs. (4.15), (4.33) and (4.34), Lagrangian of the microcantilever beam and the PZT and adsorbed biological Layer may be formulated as follows,

$$L = \frac{1}{2} \int_0^L \left\{ m(s) [\dot{u}^2 + \dot{v}^2] - EI(s) (v''^2 - 2v''^2 v'^2 - 2v''^2 u' - 2v' v'' u'') \right. \\ \left. + C_c(s) (v'' - v'' u' - v' u'' - v'' v'^2) P(t) - 4[A_1(s) - A_2(s) v'^2] \right. \\ \left. + A_3(s) v'^2 u' - A_4(s) u' \right\} + \lambda_1 [1 - (1 + u')^2 - v'^2] ds \quad (4.36)$$

where λ_1 is the Lagrangian multiplier.

Eq. (4.36) may be rewritten as

$$L = \frac{1}{2} \int_0^L l(s, t) ds \quad (4.37)$$

where function $l(s, t)$ is defined as follows,

$$l(s, t) = m(s) [\dot{u}^2 + \dot{v}^2] - C_\zeta(s) (v''^2 - 2v''^2 v'^2 - 2v''^2 u' - 2v' v'' u'') \\ + C_c(s) (v'' - v'' u' - v' u'' - v'' v'^2) P(t) - 4[A_1(s) - A_2(s) v'^2] \\ + A_3(s) v'^2 u' - A_4(s) u' + \lambda_1 [1 - (1 + u')^2 - v'^2] \quad (4.38)$$

It is known from the extended Hamilton's principle that,

$$\delta \int_{t_0}^{t_d} L dt = 0, \quad \text{where } L = L(\dot{u}, u', u'', v, \dot{v}, v', v'') \quad (4.39)$$

Substituting Eq. (4.37) into Eq. (4.39) will result as follows,

$$\begin{aligned}
\delta \int_{t_0}^{t_d} L dt = & \frac{1}{2} \int_{t_0}^{t_d} \left\{ \int_0^L \left[-\frac{d}{dt} \left(\frac{\partial l}{\partial \dot{u}} \right) - \frac{d}{ds} \left(\frac{\partial l}{\partial u'} \right) + \frac{d^2}{ds^2} \left(\frac{\partial l}{\partial u''} \right) \right] \delta u ds \right. \\
& + \int_0^L \left[-\frac{d}{dt} \left(\frac{\partial l}{\partial \dot{v}} \right) - \frac{d}{ds} \left(\frac{\partial l}{\partial v'} \right) + \frac{d^2}{ds^2} \left(\frac{\partial l}{\partial v''} \right) \right] \delta v ds \\
& + \left\{ \left[\frac{\partial l}{\partial u'} - \frac{d}{ds} \left(\frac{\partial l}{\partial u''} \right) \right]_{s=L} \right\} \delta u_L - \left[\frac{\partial l}{\partial u'} - \frac{d}{ds} \left(\frac{\partial l}{\partial u''} \right) \right]_{s=0} \delta u_0 \\
& + \left\{ \left[\frac{\partial l}{\partial v'} - \frac{d}{ds} \left(\frac{\partial l}{\partial v''} \right) \right]_{s=L} \right\} \delta v_L - \left[\frac{\partial l}{\partial v'} - \frac{d}{ds} \left(\frac{\partial l}{\partial v''} \right) \right]_{s=0} \delta v_0 \\
& + \left(\frac{\partial l}{\partial u''} \right)_{s=L} \delta u'_L - \left(\frac{\partial l}{\partial u''} \right)_{s=0} \delta u'_0 + \left(\frac{\partial l}{\partial v''} \right)_{s=L} \delta v'_L - \left(\frac{\partial l}{\partial v''} \right)_{s=0} \delta v'_0 \Big\} dt = 0
\end{aligned} \tag{4.40}$$

The partial derivatives in Eq. (4.40) are found from Eq. (4.38) as follows,

$$\frac{\partial l}{\partial \dot{u}} = 2m(s)\dot{u} \tag{4.41}$$

$$\begin{aligned}
\frac{\partial l}{\partial u'} = & -EI(s)(-2v''^2) + C_c(s)(-v'')P(t) - 4A_3(s)v'^2 \\
& + 4A_4(s) + \lambda_1(-2-2u')
\end{aligned} \tag{4.42}$$

$$\frac{\partial l}{\partial u''} = -EI(s)(-2v'v'') + C_c(s)(-v')P(t) \tag{4.43}$$

$$\frac{\partial l}{\partial \dot{v}} = 2m(s)\dot{v} \tag{4.44}$$

$$\begin{aligned}
\frac{\partial l}{\partial v'} = & -EI(s)(-4v''^2v' - 2v''u'') + C_c(s)(-u'' - 2v''v')P(t) \\
& + 8A_2(s)v' - 8A_3(s)v'u' + \lambda_1(-2v')
\end{aligned} \tag{4.45}$$

$$\frac{\partial l}{\partial v''} = -EI(s)(2v'' - 4v''v'^2 - 4v''u' - 2v'u'') + C_c(s)(1 - u' - v'^2)P(t) \quad (4.46)$$

Substituting Eqs. (4.41) to (4.46) into Eq. (4.39) and knowing that $\delta u, \delta v, \delta u_L, \delta u_0, \delta v_L, \delta v_0, \delta u'_L, \delta u'_0, \delta v'_L$ and $\delta v'_0$ are independent, the following relation may be derived,

for (δu) :

$$\begin{aligned} & -2m\ddot{u} + [EI(s)(-2v''^2)]' - [C_c(s)(-v'')P(t)]' - [\lambda_1(-2u' - 2)]' \\ & + [4A_3(s)v'^2]' - [4A_4(s)]' - [EI(s)(-2v'v'')]'' + [C_c(s)(-v')P(t)]'' = 0 \end{aligned} \quad (4.47)$$

for (δv) :

$$\begin{aligned} & -2m\ddot{v} + [EI(s)(-4v''^2v' - 2v''u'')]'' - [C_c(s)(-u'' - 2v''v')P(t)]' + [\lambda_1(2v')]'' \\ & - [8A_2(s)v']' + [8A_3(s)v'u']' - [EI(s)(2v'' - 4v''v'^2 - 4v''u' - 2v'u'')]'' \\ & + [C_c(s)(1 - u' - v'^2)P(t)]'' = 0 \end{aligned} \quad (4.48)$$

The other terms of Eq. (4.40) will be later considered as the boundary conditions of the vibrating system.

Lagrangian multiplier may be formulated from Eq. (4.47). Applying the inextensibility condition (from Eq. (4.16)), λ_1 may be formulated as follows,

$$\begin{aligned} \lambda_1 = & \int_L^s \left(-\frac{1}{2} m(s) \frac{\partial^2}{\partial t^2} \int_0^y v'^2 dx \right) dy + EI(s)(v''^2) - \frac{1}{2} C_c(s)(v'') P(t) \\ & - 2A_3(s)v'^2 + 2A_4(s) - [EI(s)(v'v'')]']' + \frac{1}{2} [C_c(s)(v')P(t)]']' = 0 \end{aligned} \quad (4.49)$$

Substituting λ_1 found in Eq. (4.49) into Eq. (4.48) and applying the inextensibility condition, Eq. (4.48) may be rewritten as follows,

$$\begin{aligned} -m\ddot{v} + & \left[v' \int_L^s \left(-\frac{1}{2} m \frac{\partial^2}{\partial t^2} \int_0^y v'^2 dx \right) dy \right]' + [EI(s)(-v''^2 v')]']' - [EI(s)(v'')]'' \\ & + [EI(s)(v'v''^2)]']' - \left\{ v' [EI(s)(v'v'')]']' \right\}' - [4A_3(s)v'^3]' + [2A_1(s)v']' \\ & + \frac{1}{2} \left[C_c(s) \left(1 - \frac{1}{2} v'^2 \right) P(t) \right]'' - \left[C_c(s) \left(-\frac{1}{2} v'' v' \right) P(t) \right]' - \frac{1}{2} [C_c(s)(v'v'')P(t)]' \\ & + \frac{1}{2} \left\{ v' [C_c(s)(v')P(t)]']' \right\}' = 0 \end{aligned} \quad (4.50)$$

Simplifying Eq. (4.50), the general equation of motion of the microcantilever depicted in Figure 4.10 can be formulated as follows,

$$\begin{aligned} -m\ddot{v} + & \left[v' \int_L^s \left(-\frac{1}{2} m \frac{\partial^2}{\partial t^2} \int_0^y v'^2 dx \right) dy \right]' - [EI(s)(v'')]'' - \left\{ v' [EI(s)(v'v'')]']' \right\}' \\ & + [2A_1(s)v']' - [4A_3(s)v'^3]' + \frac{1}{2} \left[C_c(s) \left(1 - \frac{1}{2} v'^2 \right) P(t) \right]'' \\ & + \frac{1}{2} \left\{ v' [C_c(s)(v')P(t)]']' \right\}' = 0 \end{aligned} \quad (4.51)$$

Now that the equation of motion of the microcantilever is derived, the boundary conditions will be derived in the rest of this chapter.

The geometric admissibility results in the following relation,

$$v(0, t) = 0 \quad (4.52)$$

which may be rewritten as follows,

$$\delta v_0 = 0 \quad (4.53)$$

Equations giving the boundary conditions are derived from Eq. (4.40) as follows,

for $(\delta v'_L)$:

$$\left\{ \left(\frac{\partial l}{\partial v''} \right)_{s=l} \right\} \delta v'_l = 0 \quad (4.54)$$

Substituting Eq. (4.46) into Eq. (4.54) will result in the following relation,

$$\left\{ EI(L)(-2v_L''^2) + C_c(L) \left(1 - \frac{1}{2} v_L'^2 \right) P(t) \right\} \delta v'_L = 0 \quad (4.55)$$

$\delta v'_L$ being arbitrary, Eq. (4.55) will result in the following relation,

$$EI(L)(-2v_L''^2) + C_c(L) \left(1 - \frac{1}{2} v_L'^2 \right) P(t) = 0 \quad (4.56)$$

It is derived from Eq. (4.26) that $C_c(L) = 0$. Even if the piezoelectric layer covers the whole length of the microcantilever, it is a correct assumption to consider $L - l_2 = \varepsilon$. Thus, Eq. (4.56) reduces to the following equation,

$$EI(L)(-2v_L''^2) = 0 \quad (4.57)$$

Knowing that $EI(L) \neq 0$ the following relation may be concluded,

$$v_L'' = 0 \quad (4.58)$$

for (δv_L) :

$$\left\{ \left[\frac{1}{2} \frac{\partial l}{\partial v'} - \frac{1}{2} \frac{d}{ds} \left(\frac{\partial l}{\partial v''} \right) \right]_{s=L} \right\} \delta v_L = 0 \quad (4.59)$$

Substituting Eqs. (4.25) and (4.46) into Eq. (4.59) the following equation may be formulated,

$$\left\{ -EI(L)(-2v_L''^2 v_L') + C_c(L)(-v_L'' v_L') P(t) + \lambda_1(-2v_L') \right. \\ \left. - \left[-EI(s)(2v'') \right]_{s=L}' + \left[C_c(s) \left(1 - \frac{1}{2} v'^2 \right) P(t) \right]_{s=L}' \right\} \delta v_L = 0 \quad (4.60)$$

δv_L being arbitrary, Eq. (4.60) will result in the following relation,

$$-EI(L)(-2v_L''^2 v_L') + C_c(L)(-v_L'' v_L') P(t) + \lambda_1(-2v_L') \\ - \left[-EI(s)(2v'') \right]_{s=L}' + \left[C_c(s) \left(1 - \frac{1}{2} v'^2 \right) P(t) \right]_{s=L}' = 0 \quad (4.61)$$

Assuming $EI'(s)$ and $C_c'(s)$ are zero and considering Eq. (4.58), Eq.

(4.61) will be rewritten as follows,

$$EI(L)v_L'''(v_L'^2 + 1) = 0 \quad (4.62)$$

Therefore, the second boundary condition at $s=L$ will be found from Eq. (4.62) as follows,

$$v_L''' = 0 \quad (4.63)$$

for (δv_0) :

$$\left[\frac{1}{2} \frac{\partial l}{\partial v'} - \frac{1}{2} \frac{d}{ds} \left(\frac{\partial l}{\partial v''} \right) \right]_{s=0} \delta v_0 = 0 \quad (4.64)$$

Having $\delta v_0 = 0$ from Eq. (4.53), Eq. (4.64) doesn't result in a new boundary condition.

for $(\delta v_0')$:

$$\left\{ \left(\frac{\partial l}{\partial v''} \right)_{s=0} \right\} \delta v_0' = 0 \quad (4.65)$$

Substituting Eq. (4.46) into Eq. (4.65) will result in the following relation,

$$\left\{ EI(0)(-2v_0''^2) + C_c(0) \left(1 - \frac{1}{2} v_0'^2 \right) P(t) \right\} \delta v_0' = 0 \quad (4.66)$$

Assuming $\delta v_0'$ is arbitrary, Eq. (4.66) will give the following equation,

$$EI(0)(-2v_0''^2) + C_c(0)\left(1 - \frac{1}{2}v_0'^2\right)P(t) = 0 \quad (4.67)$$

It is derived from Eq. (4.26) that $C_c(0) = 0$. Even if the piezoelectric layer covers the whole length of the microcantilever, it is a correct assumption to consider $l_1 = \varepsilon$. Thus, Eq. (4.67) reduces to the following,

$$EI(0)(-2v_0''^2) = 0 \quad (4.68)$$

However, it is concluded from Eq. (4.17) that $EI(0) \neq 0$ and also due to the nonzero moment at $s=0$, $v_0'' \neq 0$. This means that Eq. (4.67) may not be satisfied unless $\delta v_0'$ equals zero,

$$\delta v_0' = 0 \Rightarrow v_0' = 0 \quad (4.69)$$

Thus, the general equation of motion and the boundary conditions of the vibrating microcantilever beam depicted in Figure 4.10 will be as follows,

$$\begin{aligned} & -m\ddot{v} + \left[v' \int_L^s \left(-\frac{1}{2} m \frac{\partial^2}{\partial t^2} \int_0^y v'^2 dx \right) dy \right]' - [EI(s)(v'')]'' - \left\{ v' [EI(s)(v'v'')] \right\}' \\ & + [2A_1(s)v']' - [4A_3(s)v'^3]' + \frac{1}{2} \left[C_c(s) \left(1 - \frac{1}{2} v'^2 \right) P(t) \right]'' \\ & + \frac{1}{2} \left\{ v' [C_c(s)(v')P(t)] \right\}' = 0 \end{aligned} \quad (4.70)$$

At $s=0$:

$$v = v' = 0 \quad (4.71)$$

At $s=L$:

$$v'' = v''' = 0 \quad (4.72)$$

CHAPTER 5

SOLUTION TO THE NONLINEAR EQUATIONS OF MOTION OF THE MICROCANTILEVER

The nonlinear equation of motion of the piezoelectrically-driven microcantilever beam with a layer of the adsorbed biological species, depicted schematically in Figure 4.10 (a), was derived in the previous chapter, Eq. (4.70), with the boundary conditions of Eqs. (4.71) and (4.72).

The beam deflection, $v(s, t)$, can be truncated into n -modes as follows,

$$v(s, t) = \sum_{i=1}^n v_i(s, t) = \sum_{i=1}^n \phi_i(s) q_i(t) \quad (5.1)$$

where ϕ_i is the comparison function (satisfying only the boundary conditions and not necessarily the equations of motion) and q_i is the generalized time-dependent coordinate for i^{th} mode of the beam. For the cantilever boundary conditions considered in Eqs. (4.71) and (4.72), the following linear mode shapes of bending are considered

$$\phi_i(s) = A_i \left\{ \cosh(\lambda_i s) - \cos(\lambda_i s) + [\sin(\lambda_i s) - \sinh(\lambda_i s)] \frac{\cosh(\lambda_i L) + \cos(\lambda_i L)}{\sin(\lambda_i L) + \sinh(\lambda_i L)} \right\} \quad (5.2)$$

where λ_i are the roots of the following frequency equation,

$$1 + \cos(\lambda_i L) \cosh(\lambda_i L) = 0 \quad (5.3)$$

and A_i is a constant being obtained using the orthogonality condition (of the mode shapes).

Substituting Eqs. (5.1) and (5.2) into Eq. (4.70) and taking the inner product of the resulting equation with $\phi_i(s)$ yields the following ordinary differential equation for $q_i(t)$

$$g_{1i} \ddot{q}_i + g_{2i} \dot{q}_i + g_{3i} q_i^3 + g_{4i} (q_i^2 \ddot{q}_i + q_i \dot{q}_i^2) - g_{5i} q_i^2 P(t) = g_{6i} P(t) \quad (5.4)$$

where

$$g_{1i} = \int_0^L m(s) \phi_i^2(s) ds \quad (5.5)$$

$$g_{2i} = \int_0^L \left[\phi_i(s) (EI(s) \phi_i''(s))' - (2A_1(s) \phi_i'(s))' \right] ds \quad (5.6)$$

$$g_{3i} = \int_0^L \left[\phi_i(s) (EI(s) \phi_i'(s) \phi_i''(s))' + \phi_i(s) (EI(s) \phi_i'^2(s) \phi_i''(s))' + 4\phi_i(s) (A_3(s) \phi_i'^3(s))' \right] ds \quad (5.7)$$

$$g_{4i} = \int_0^L m\phi_i(s) \left[\phi_i'(s) \int_0^s \int_0^y 2\phi_i'^2(x) dx dy \right]' ds \quad (5.8)$$

$$g_{5i} = \int_0^L \phi_i(s) (C_c(s) \phi_i'(s) \phi_i''(s))' ds + \frac{1}{2} \int_0^L \phi_i(s) (C_c(s) \phi_i'^2(s))'' ds \quad (5.9)$$

$$g_{6i} = \frac{1}{2} \int_0^L \phi_i(s) C_c''(s) ds \quad (5.10)$$

Using Eq. (5.4), the nonlinear equation of motion of the microcantilever given in Eq. (4.70) can be simulated using Matlab[®]/Simulink[®]. The Matlab code and simulation diagrams are both given in Appendix A. Results and discussions of the simulation are discussed in the following sections.

Numerical Simulations and Results

Considering the general equation of motion of the microcantilever given in Eq. (4.70) or its discretized version given by Eq. (5.4), the resonance frequency of the PZT-driven microcantilever with the adsorbed biological species can be found. In order to run the simulation for deriving the solution to Eq. (5.4), structural properties of the microcantilever beam and the attached PZT layer together with Lennard-Jones constants and molecular spacing of the adsorbed biological species are needed. The microcantilever and the PZT layer considered here and in the simulations have the following properties,

Beam:	L (length) = 500 μm	PZT Layer:	L (length) = 500 μm
	w (width) = 100 μm		w (width) = 100 μm
	t (thickness) = 1 μm		t (thickness) = 0.5 μm
	$\nu = 0.23$		$\nu = 0.25$
	$E = 170 \text{ GPa}$		$E = 133 \text{ GPa}$
	$\rho = 2330 \text{ kg/m}^3$		$\rho \cong 6390 \text{ kg/m}^3$

(5.11)

The Lennard-Jones constants and molecular spacing of the biological species are also needed. As mentioned earlier, it is not easy to find the Lennard-Jones constants of biological species. The Lennard-Jones constants for different molecular structures vary in the range of $A=2\times 10^{-79}$ to $1\times 10^{-76} \text{ J.m}^6$ and $B=2\times 10^{-136}$ to $4\times 10^{-134} \text{ J.m}^{12}$ [11, 71]. There exist different tables of the Lennard-Jones constants for gases, however, these constants are found empirically for each biological species in the desired conditions.

In our modeling, in order to have an estimate of these Lennard-Jones constants and due to the fact that there were no in-house experimental results available, the McFarland *et al.*'s results [42] were utilized and the inverse engineering was performed. This is done in order to obtain the resonance frequency shifts as measured in McFarland *et al.* experiment. Hence, the following physical properties of microcantilever beam are considered here.

$$\begin{aligned}
L \text{ (length)} &= 500 \mu\text{m} \\
w \text{ (width)} &= 100 \mu\text{m} \\
t_b \text{ (thickness)} &= 1 \mu\text{m} \\
\nu &= 0.23 \\
E &= 170 \text{ GPa} \\
\rho &= 2330 \text{ kg/m}^3
\end{aligned}
\tag{5.12}$$

These parameters are nominal values as reported by McFarland *et al.* [42] It is mentioned in McFarland *et al.* results that the actual values for length, width and thickness of the beam are 499 μm , 97 μm and 0.8 μm , respectively. Hence, these values are used in our simulations in order to be in accordance with these experiments.

In McFarland *et al.* experiment, no PZT patch has been attached to the surface of the microcantilever. Hence, in order to find the properties of the adsorbed biological species, it is assumed here that no PZT is attached to the microcantilever surface and the simulations are done.

Performing the simulations for this microcantilever beam, its resonance frequency before the adsorption of biological species is found to be 4549 Hz. Having the initial natural frequency of microcantilever, constants A and B are changed until the desired frequency shift is obtained (assuming the molecular distance is constant and equal to 0.5 nm). McFarland *et al.* frequency shifts for three different beams are listed in Table 5.1. From this table, we choose the desired shift of frequency to be in the range of 20-30 Hz.

Table 5.1: Experimental resonance frequencies before (f_l), and after adsorption (f_{ads}), and the variation in microcantilever's resonance frequency (Δ) [42]

Beam Number	f_l (kHz)	f_{ads} (kHz)	Δ (Hz)
1	4.56	4.57	10
2	4.55	4.59	40
3	4.62	4.64	20

Based on McFarland *et al.* experimental data, the simulations and reverse calculations have been performed for such values of A and B that result in a shift in the resonant frequency of about 20-30 Hz. A number of simulations were done with the best results for constants A and B provided in Table 5.2.

Table 5.2: Simulation results for constants A and B and the corresponding frequency

A (J.m ⁶)	B (J.m ¹²)	f (Hz)	Δ (Hz)
0	0	4552	0
0.7×10^{-72}	0.3×10^{-135}	4563	11
1×10^{-72}	0.4×10^{-135}	4574	22
1.3×10^{-72}	0.4×10^{-135}	4586	34

These results show that for a range of $A=0.7 \times 10^{-72}$ to $A=1.3 \times 10^{-72}$ J.m⁶ and $B=0.3 \times 10^{-135}$ to $B=0.4 \times 10^{-135}$ J.m¹², the parameter Δ varies from 11Hz to 34Hz which is almost the desired range

One pair of possible Lennard-Jones constants are found as follows,

$$A=1.3 \times 10^{-72} \text{ J.m}^6 \text{ and } B=0.4 \times 10^{-135} \text{ J.m}^{12}, \quad (5.13)$$

satisfying the desired shift of resonance frequency. The frequency response for this pair of Lennard-Jones constants is depicted in Figure 5.1. Through the rest of the simulations, these two constants are considered for the adsorbed biological species.

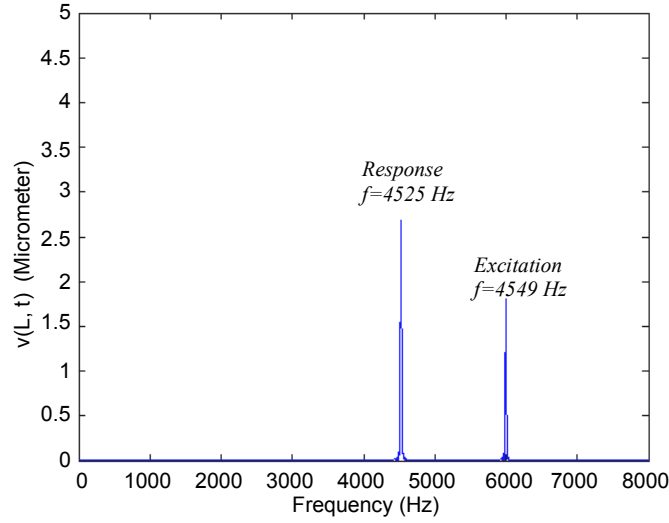


Figure 5.1: Frequency response of a microcantilever with properties listed in Eq. (5.12) and the adsorbed biological species on its surface having Lennard-Jones constants of $A=1.3 \times 10^{-72} \text{ J.m}^6$ and $B=0.4 \times 10^{-135} \text{ J.m}^{12}$

The obtained constants A and B , however, do not match the typical range for molecules (and biological species). It should be mentioned that the intermolecular forces of attraction/repulsion are not the only adhesion forces present. Our results clearly show that other adhesion forces such as electrostatic interactions have non-negligible effects on the resonance response of the system. It is also demonstrated that there exist other sources accounting for the surface stress such as the surface charge redistribution of the underlying substrate. This may have a dominant role in the resonance frequency shift of the microcantilever [42]. It is important to mention that these effects are even more dominant than the attraction/repulsion effect, since the Lennard-Jones constants found here are far beyond the reality. Therefore, the obtained constants need to be refurbished by considering the mentioned forces and effects in further investigations.

Remark: The value of b as mentioned in Chapter 4 depends on the concentration of the solution. We assume this parameter to be 0.5 nm and will later (in the following sections) study how it is related to the resonance frequency of microcantilever beam.

As mentioned earlier in this section, the resonance frequency of the vibrating microcantilever may be numerically derived from Eq. (5.4). In the following sections, the effects of the adsorbed biological and the attached PZT layers on the resonance frequency of microcantilever beam are investigated. The nonlinear terms and their influence on the frequency response of the system are first studied for the case where there is no biological layer adsorbed on the surface of the microcantilever (before the adsorption); hence, only the effect of the attached PZT layer is investigated. Having the effect of PZT layer on the shift in the frequency studied, it is assumed that the biological layer is adsorbed and the effect of both layers is investigated on the shift in the resonance frequency of the vibrating microcantilever.

The Effect of the Attached PZT Layer

Unlike the biological layer with its thickness and rigidity being negligible, the attached PZT layer is thick enough to change the rigidity of the system. Considering the microcantilever studied before, a PZT layer with the properties listed in Eq. (5.11) is considered to be attached on its surface.

In the first step, we will only consider the effect of linear terms on frequency response of the system, thus, the coefficients of nonlinear terms are considered to be zero. A voltage of 1V with frequency of excitation of 9 kHz is applied to the PZT actuator to obtain the linear frequency. Figure 5.2 shows the response of the system with the added PZT layer. It is indicated that its resonance appears at the frequency of 8248 Hz (which is much higher than the resonance frequency of the microcantilever without the piezoelectric layer).

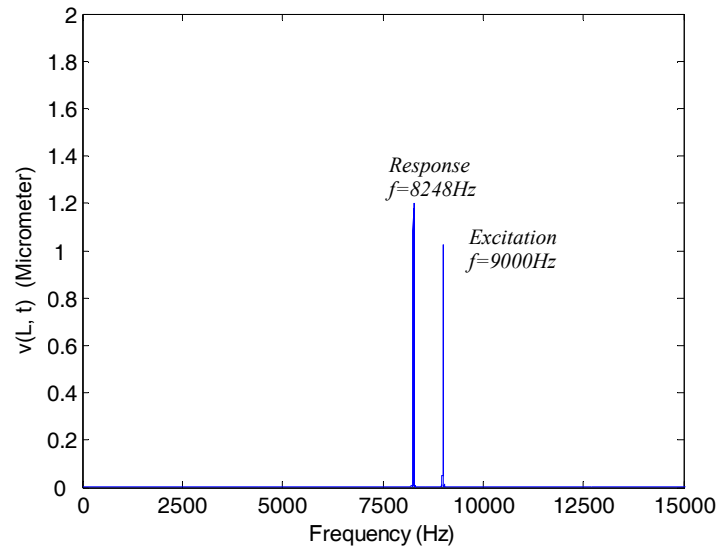


Figure 5.2: Linear frequency response of the PZT-driven microcantilever

The nonlinear terms are now considered in the simulations and the numerical frequency response is calculated again. The values of the exciting voltage are considered to be the same as the excitation for linear frequency response. The obtained nonlinear frequency response is depicted in Figure 5.3.

When linear and nonlinear frequency responses are compared, it is observed that there exists roughly 14 Hz of shift in the frequency responses. This amount may seem to be rather small. However, this difference is in the measurable range of the microcantilever sensors, and hence, important for accurate measurement. Hence, it is important that the nonlinearity of the microcantilever's structure and the attached PZT layer be considered in the resonance response measurements.

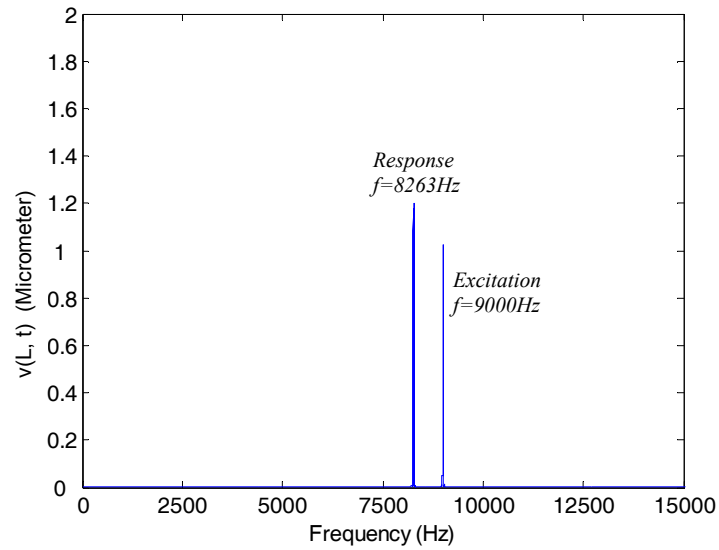


Figure 5.3: Nonlinear frequency response of the PZT-driven microcantilever

The Effect of Both PZT and the Adsorbed Biological Layers

In our simulations, it was observed that considering the biological layer effect on the resonance frequency shift in the presence of PZT layer, highly depends on the geometry of the system. For the original microcantilever with

length, width and thickness of 500 μm , 100 μm and 1 μm , respectively, and with no PZT layer, a shift in the range of 11 to 34 Hz was induced, depending on the Lennard-Jones constants (see Table 5.2). However, this shift further decreases if the PZT layer is added to the microcantilever, as listed in Table 5.3 and depicted in Figure 5.4 for $A=1.3\times 10^{-72}$ J.m⁶ and $B=0.4\times 10^{-135}$ J.m¹².

Table 5.3: Simulation results for constants A and B and the corresponding frequencies for PZT-driven microcantilever

A (J.m ⁶)	B (J.m ¹²)	f (Hz)	Δ (Hz)
0	0	8262	0
0.7×10^{-72}	0.3×10^{-135}	8265	3
1×10^{-72}	0.4×10^{-135}	8267	5
1.3×10^{-72}	0.4×10^{-135}	8268	6

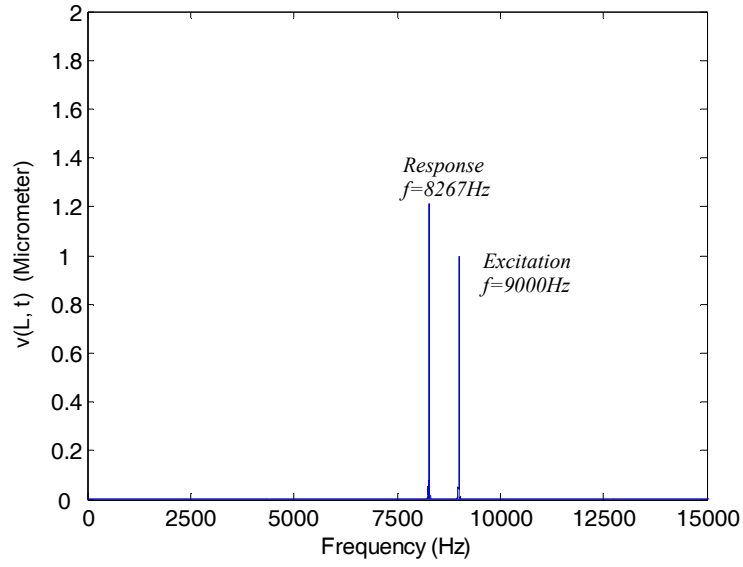


Figure 5.4: Nonlinear frequency response of the PZT-driven microcantilever covered by a biological layer with $A=1 \times 10^{-72} \text{ J.m}^6$ and $B=0.4 \times 10^{135} \text{ J.m}^{12}$

This demonstrates that adding a PZT layer with half the thickness of the microcantilever result in a thicker beam, and hence the molecular surface stress of the adsorbed biological species will have less effect on the frequency response of the system. This indicates that there exist limitations on the structural geometry of the microcantilever in order to be applicable for biosensing.

CHAPTER 6

SENSITIVITY STUDY OF THE STATIC MODE DETECTION

The nonlinear equation of motion of the PZT-driven microcantilever biosensor of Figure 4.10, Eq. (4.70), was solved in Chapter 5 by first discretizing the equation of motion and applying the Galerkin method and numerically solving the derived ordinary differential equations of motion of the microcantilever. In this Chapter, a new approach is introduced towards the solution of the equation of motion (4.70). This new approach is utilized in formulating the static deflection of the microcantilever and as a result, the sensitivity of this formulated static deflection detection mode is compared to that of the dynamic mode formulated in Chapter 5.

This method of formulating the static deflection is a powerful method as it formulates all the intermolecular forces causing the surface stress into the general equation of motion of the microcantilever. It is easy and straightforward to bring the forces into the equation of motion of the microcantilever by just knowing its potential.

A New Approach toward Solution of the Nonlinear Equation of Motion of Eq. (4.70)

The nonlinear vibration of the microcantilever given in Eq. (4.70) can be considered as the linear vibrations of the microcantilever around its statically deflected position. In other words, the transversal displacement of the microcantilever, $v(s, t)$, can be written as,

$$v(s, t) = v_s(s) + v_{Linear}(s, t) \quad (6.1)$$

where $v_s(s)$ is the static deflection of the beam. The difference between this method and the method of previous chapter is that the special function $\phi_n(s)$ of the equation of motion of the vibrating microcantilever is no longer a comparison function, instead the eigenfunction of the beam satisfying both boundary conditions and the equation of motion of the linear vibrating beam.

The static deflection of Eq. (6.1) may be easily found by ignoring the time-varying terms in Eq. (4.70), which results in an equation as follows,

$$-[EI(s)(v_s'')]' - \left\{ v' [EI(s)(v_s' v_s'')] \right\}' + [2A_1(s)v_s']' - [4A_3(s)v_s'^3]' = 0 \quad (6.2)$$

Similar to the assumption made in Chapter 5, it is assumed that $EI(s)$, $A_1(s)$ and $A_3(s)$ are constants, hence their derivatives will vanish when expanding Eq. (6.2).

In order to solve Eq. (6.2) and find the static deflection of the microcantilever beam, Eq. (6.2) needs to be non-dimensionalized first. In this regard, the new non-dimensional variables x and $\hat{v}_s(x)$ are defined as follows,

$$\begin{aligned} x &\triangleq \frac{s}{L} \\ \Rightarrow v_s(s) &= v_s(xL) = \hat{v}_1(x) \end{aligned} \quad (6.3)$$

$$\hat{v}_s(x) \triangleq \frac{\hat{v}_1(x)}{L} \quad (6.4)$$

Substituting Eqs. (6.3) and (6.4) into Eq. (6.2) and taking the derivatives, the equation of the static deflection can be rewritten as follows,

$$-B_1 \left[\hat{v}_s'''' \left(1 + \hat{v}_s'^2 \right) + \hat{v}_s'''^3 + 4\hat{v}_s''' \hat{v}_s'' \hat{v}_s' \right] + B_2 \hat{v}_s'' - B_3 \hat{v}_s'' \hat{v}_s'^2 = 0 \quad (6.5)$$

with the boundary conditions of

at $x=0$:

$$\hat{v}_s = \hat{v}_s' = 0 \quad (6.6)$$

at $x=L$:

$$\hat{v}_s'' = \hat{v}_s''' = 0 \quad (6.7)$$

where

$$B_1 = \frac{EI}{L^3} \quad (6.8)$$

$$B_2 = \frac{2A_1}{L} \quad (6.9)$$

$$B_3 = \frac{12A_3}{L} \quad (6.10)$$

Only two of the four boundary conditions listed in Eqs. (6.6) and (6.7) are available at $x=0$. Hence, in order to solve Eq. (6.5) the “shooting method” will be utilized. Using this method, the two unavailable initial conditions at $x=0$ are assumed to be known as $\hat{v}_s''(0) = \alpha$ and $\hat{v}_s'''(0) = \beta$, where α and β are some constants to be determined. Having all four initial conditions, the static deflection of the microcantilever may be found numerically based on the following equation,

$$\begin{aligned} y_1 &= \hat{v}_s \\ y_2 &= \hat{v}_s' = y_1' \\ y_3 &= \hat{v}_s'' = y_2' \\ y_4 &= \hat{v}_s''' = y_3' \\ y_4' &= \hat{v}_s^{(4)} = \frac{-\left(\frac{B_3}{B_1}\right)y_3y_2^2 + \left(\frac{B_2}{B_1}\right)y_3 - y_3^3 - 4y_4y_3y_2}{1 + y_2^2} \end{aligned} \quad (6.11)$$

with the initial conditions as follows,

$$\begin{aligned}
y_1(0) &= 0 \\
y_2(0) &= 0 \\
y_3(0) &= \alpha \\
y_4(0) &= \beta
\end{aligned} \tag{6.12}$$

The values of α and β are found by trial and error, i.e., they are changed until the original boundary conditions of $\hat{v}_s'' = \hat{v}_s''' = 0$ are satisfied at the free end of the microcantilever.

Numerical Simulations and Results

The properties of the microcantilever beam, the PZT layer and the adsorbed biological species (monolayer of thiol molecules) considered in the simulations are those derived and listed in Eqs. (5.13) and (5.11) as follows,

<p>Beam:</p> <p>L (length) = 500 μm</p> <p>w (width) = 100 μm</p> <p>t (thickness) = 1 μm</p> <p>$\nu = 0.23$</p> <p>$E = 170 \text{ GPa}$</p> <p>$\rho = 2330 \text{ kg/m}^3$</p>	<p>PZT Layer:</p> <p>L (length) = 500 μm</p> <p>w (width) = 100 μm</p> <p>t (thickness) = 0.5 μm</p> <p>$\nu = 0.25$</p> <p>$E = 133 \text{ GPa}$</p> <p>$\rho \cong 6390 \text{ kg/m}^3$</p>
--	---

(6.13)

Biological Layer: $A = 1.3 \times 10^{-72} \text{ J.m}^6$, $B = 0.4 \times 10^{-135} \text{ J.m}^{12}$ (6.14)

As described in the previous section, shooting method is applied for the static deflection formulation. By trial and error, the appropriate α and β for the

system with the properties listed in Eqs. (6.13) and (6.14) are found as $\alpha = -1$ and $\beta = 1.05$. The static deflection of the microcantilever is then found numerically for these two values of α and β as depicted in Figure 6.1.

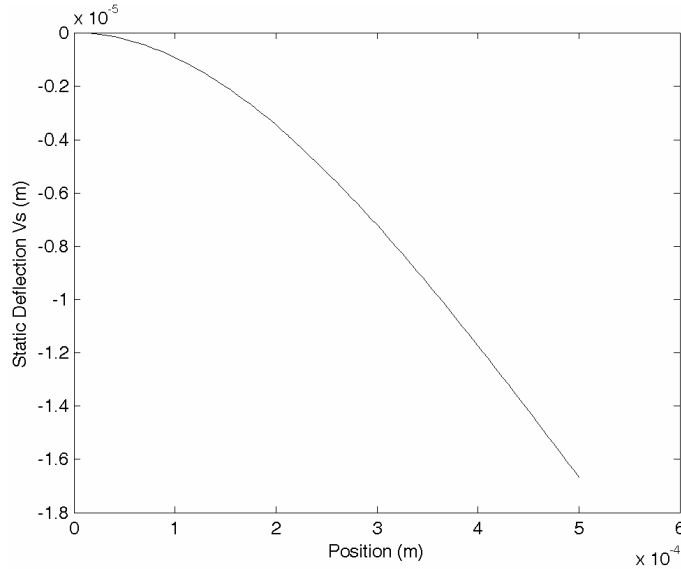


Figure 6.1: The static deflection of the microcantilever with length=500 (μm), width= 100 (μm) and thickness=1 (μm)

It is also demonstrated in Figure 6.2 that if all the properties of the system remains unchanged, microcantilever's tip deflection varies almost linearly by varying its length, especially for the larger lengths. The properties of the five microcantilevers depicted in Figure 6.2 are the same as those listed in Eqs. (6.13) and (6.14) except for the width. The width is considered to be 10 μm so that reducing the length of the microcantilever doesn't violate the assumptions of the Euler- Bernoulli beam.

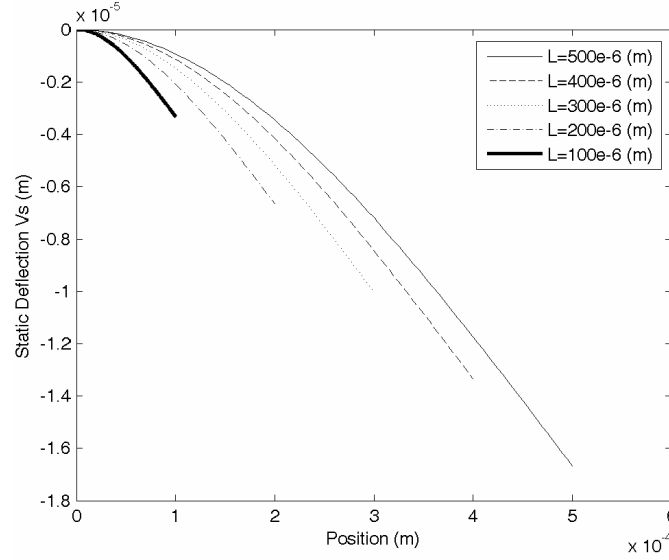


Figure 6.2: The static deflection of five microcantilever beams differing only in their lengths

Sensitivity of the Static vs. the Dynamic Detection Mode

Figure 6.2 depicts the change in the static deflection of the microcantilever while the only property being altered is the length of the beam. In order to find the sensitivity of the static deflection detection mode to the adsorbed biological species, the properties of the microcantilever beam and the PZT layer on its surface are kept unchanged and the Lennard-Jones constants of the adsorbed biological species are varied.

It is depicted in Figure 6.3 how the static deflection of the PZT-driven microcantilever with properties listed in Eqs. (6.13) and (6.14) varies by varying the Lennard-Jones constant A of the adsorbed species. Constant A is varied from 1.3×10^{-72} to 1.3×10^{-63} . It is observed that even by increasing A to 1.3×10^{-66} (which

is quite a large number for A constant) there will be no significant change in the static deflection; hence the static deflection formulated in the present chapter is not much sensitive to the change in the properties of the adsorbed biological species.

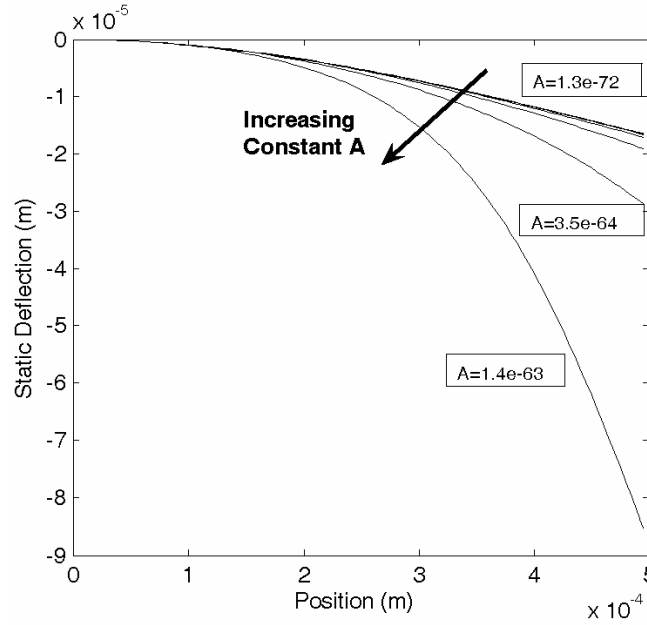


Figure 6.3: Different static deflections of the PZT-driven microcantilever with the properties listed in Eqs. (6.13) and (6.14) for different Lennard-Jones A constants

The effect of the change in the properties of the adsorbed species on the frequency response of the system is also depicted in Figure 6.4. It needs to be considered that this response is found for the first mode of vibration of the microcantilever applying the approach explained in Chapter 5. It is clearly observed that by increasing constant A to 1.3×10^{-70} the resonance frequency of the microcantilever shifts by a large, measurable value of 290 Hz.

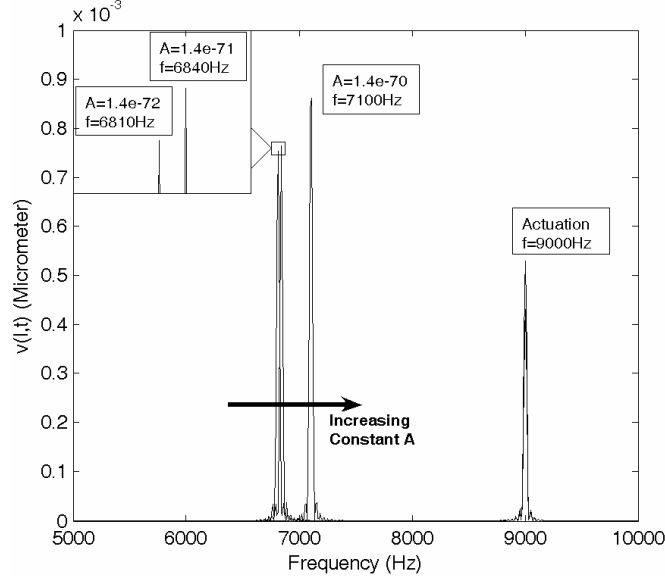


Figure 6.4: Resonance frequencies of the first mode of vibration for the PZT-driven microcantilever with the properties listed in Eqs. (6.13) and (6.14) for different Lennard-Jones A constants

It is clearly observed from Figures 6.3 and 6.4 that the dynamic mode of detection of the adsorbed biological species derived using the method of Chapter 5, while only considering the attraction/repulsion forces as the major factor in the microcantilever's vibration/deflection, is more sensitive compared to the static deflection mode formulated in the present chapter.

CHAPTER 7

CONCLUSIONS AND FUTURE WORK

Conclusions

Nonlinear vibrations of a piezoelectrically-driven microcantilever beam in presence of a biological monolayer were investigated and the corresponding equations of motion were derived and simulated. In formulating the general equations of motion of the beam, both linear and nonlinear terms due to the microcantilever's geometry were present. Moreover, the attached piezoelectric layer and the adsorbed biological layer produced new nonlinear terms. Two new nonlinear terms due to presence of these layers were derived and introduced in the present modeling framework.

It was concluded that the intermolecular forces of attraction/repulsion play a less dominant role on the adsorption induced surface stress and the resonance frequency shift. It was then proposed that other effects such as the electrostatic adhesion forces or the surface charge redistribution of the underlying substrate may be the contributing factors on the surface stress. It was also observed that adding the piezoelectric layer causes a great resonance frequency shift from the initial resonance frequency. Taking the nonlinearities into account causes a small shift in the resonance frequency of the system. Despite the shift being small

compared to the linear shift in resonance frequency, it is in the measurable range of the microcantilever sensors. Hence, the nonlinear effect of piezoelectric layer was shown to be important for the resonance response calculations of the system. In presence of both piezoelectric and biological layers, it was observed that the addition of piezoelectric layer on the surface of the microcantilever dominates the effect of intermolecular forces on the resonance frequency shift of the system. However, piezoelectrically-actuated microcantilever provides the ability of indirect sensing through this layer, instead of using laser sensor.

In the last phase of the present paper, a new approach was proposed for equating the static deflection of the microcantilever beam due to the adsorption-induced surface stress. It was then depicted that the proposed dynamic mode of detection of the adsorbed biological species derived, while only considering the attraction/repulsion forces as the major factor in the microcantilever's vibration/deflection, is more sensitive compared to the static deflection mode formulated in the present chapter.

Future Work and Directions

It needs to be noted that the aim of the current study is just to create a new research pathway for the problem of biologically-induced surface stress sensing when piezoelectric and geometrical nonlinearities are considered. There is the need for extensive experiments in order to verify the theoretical and numerical

results. The functionalization unit (depicted schematically in Figure 7.1) will be used in culturing the surface of microcantilever biosensors with desired target molecules. An imaging system is required in order to make sure the biological species have been adsorbed on microcantilever surface.



Figure 7.1: Cantisense functionalisation unit

The micro system analyzer (MSA-400, depicted in Figure 7.2) will be used for measuring and analyzing the frequency response of the vibrating microcantilever biosensor.

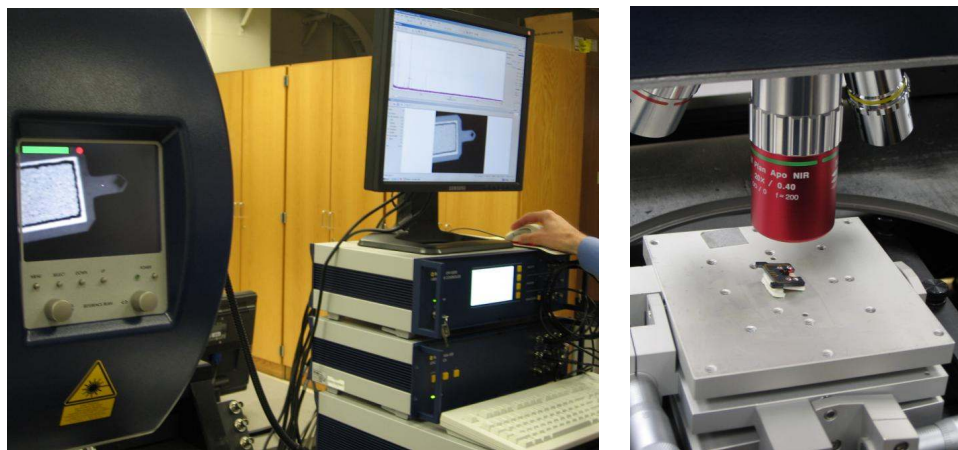


Figure 7.2: Polytec state-of-the-art Micro System Analyzer MSA 400

Figure A.1: Simulink[®] block diagram of deriving the frequency response of the vibrating microcantilever beam

The Matlab[®] code used for measuring the constants of g_I to g_6 is also given as follows.

```
close all; clear all; clc;
format long e;

wb = 100e-6;           %Beam width
wp = 100e-6;           %Piezoelectric layer width
hp = 1e-6;             %Thickness of the piezoelectric layer
hb = 1e-6;             %Thickness of beam

l1 = 0;                %Length from clamped end to beginning of
                        %the piezoelectric layer
l2 = 500e-6;           %Length of the piezoelectric layer
l3 = 0;                %Length from clamped end to beginning of
                        %the piezoelectric layer
l4 = 500e-6;           %Length of the piezoelectric layer
l = 500e-6;            %Length of beam

nup= 0.25;             %ZnO (Piezoelectric) Poisson's ratio
Ep = 133e9/(1-nup^2);  %ZnO (Piezoelectric) Modulus of
                        %elasticity
nub= 0.23;             %Beam Poisson's ratio
Eb = 170e9/(1-nub^2);  %Beam Modulus of elasticity

rb = 2330.00;          %Beam density
dens = (0.25*(19320)+3.5*(5605)+0.25*(4500))/4; %Density Au:19320
                                                %ZnO:5605 Ti:4500
rp = dens;             %Piezoelectric layer density
mb = rb*wb*hb;         %Mass per length of beam
mp = rp*wp*hp;         %Mass per length of piezoelectric layer

d31 = 11e-12;          %Piezoelectric layer compliance parameter

% System parameters

yn = (wp*hp*Ep*(hp+hb))/(2*Eb*hb*wb+2*Ep*hp*wp);

iy = hb*wb^3/12;
iyp = hp*wp^3/12;

iz = 1/12*wb*hb^3;
izb = wb*yn^2*hb+iz;
izp = wp*((hp)*yn^2-((hp+1/2*hb)^2-
1/4*hb^2)*yn+1/3*(hp+1/2*hb)^3);

id = wp*(0.5*hp^2+0.125*hb^2+yn*(0.5*hb-hp))/hp;

dt=1e-6;
s=[dt:dt:1-dt];
n=length(s);
```

```

% Lennard Jones Coefficients

b = 0.5*10^-9; AA = 1.3e-72;
BB = 4e-136;

K1 = -(heaviside(s-l3)-heaviside(s-l4))*(AA/b^7-BB/b^13);
K2 = -(heaviside(s-l3)-heaviside(s-l4))*(27*AA/b^7-90*BB/b^13);

% Mass and stiffness coefficients

m = (heaviside(s-0)-heaviside(s-l1))*mb+...
    (heaviside(s-l1)-heaviside(s-l2))*(mb+mp+ms);

cz = ((heaviside(s)-heaviside(s-l1))*Eb*iz+...
    (heaviside(s-l1)-heaviside(s-l2))*Eb*izb+...
    (heaviside(s-l1)-heaviside(s-l2))*Ep*izp);

cc=(heaviside(s-l1)-heaviside(s-l2))*Ep*d31*id;

v=0; nm=1; qout=0;

zz(1) = 3750;
zz(2) = 9388;
zz(3) = 15709.5;

for zcounter=1:nm

    ba = 0;
    z = zz(zcounter);

    for i=1:n-1
        ba = 0.5*(m(i)*(cosh(z*i*dt)-
cos(z*i*dt)+(sin(z*i*dt)-sinh(z*i*dt))*(cosh(z*1)+...
cos(z*1))/(sinh(z*1)+sin(z*1)))^2+m(i+1)*(cosh(z*(i+1)*dt)-
cos(z*(i+1)*dt)+...
        (sin(z*(i+1)*dt)-
sinh(z*(i+1)*dt))*(cosh(z*1)+cos(z*1))/(sinh(z*1)+...
        sin(z*1)))^2)*dt + ba;
    end;
    ba = sqrt(1/ba);

    beta = ba*(cosh(z*s)-cos(z*s)+(sin(z*s)-
sinh(z*s))*(cosh(z*1)+cos(z*1))/(sinh(z*1)+...
        sin(z*1)));
    betal = ba*(sinh(z*s)*z+sin(z*s)*z+(cos(z*s)*z-
cosh(z*s)*z)*(cosh(z*1)+cos(z*1))/...
        (sinh(z*1)+sin(z*1)));
    beta2 = ba*(cosh(z*s)*z^2+cos(z*s)*z^2+(-sin(z*s)*z^2-
sinh(z*s)*z^2)*(cosh(z*1)+...
        cos(z*1))/(sinh(z*1)+sin(z*1)));

```

```

g2d1 = diff(diff(cz.*beta2)/dt)/dt;
g2d2 = diff(2*K1.*beta1)/dt;
g3d1 = diff(cz.*beta1.*beta2.*beta2)/dt;
g3d2 = diff(diff(cz.*beta1.*beta1.*beta2)/dt)/dt;
g3d3 = 4*diff(K2.*beta1.^3)/dt;
g4d1 = -0.00066666666667*exp(-
7500*s).* (2.505832817*10^12*exp(-1.875000000+7500*s)+...
3.842419143*10^11*exp(1.875000000+7500*s)-
5.432106822*10^11+...
1.277243178*10^10*exp(3.750000000+7500*s)+1.081842602*10^12*exp(7
500*s)...
+5.432106822*10^11*exp(-
3.750000000+7500*s)+2.506024275*10^12*exp(3750*s).*cos(3750*s)...
-1.839661185*10^12*sin(3750*s).*exp(3750*s)-
1.095165960*10^19*s.^2.*exp(7500*s)+...
1.060876501*10^12*cos(3750*s).*sin(3750*s).*exp(7500*s)+3.9782868
79*10^15*s.*exp(7500*s)-...
3.331815452*10^11*(cos(3750*s)).^2.*exp(7500*s)+3.842712723*10^11
*exp(11250*s).*cos(3750*s)...
-2.820918181*10^11*sin(3750*s).*exp(11250*s)-
1.277243178*10^10*exp(15000*s));
g4d2 = diff(m.*beta1.*g4d1)/dt;
g5d1 = diff(cc.*beta1.*beta2)/dt;
g5d2 = diff(diff(cc.*beta1.*beta1)/dt)/dt;
g6d = diff(diff(cc)/dt)/dt;

g1 = 0; g2 = 0; g3 = 0; g4 =0; g5 = 0; g6 = 0;

for i=1:n-3

    g1 = g1 + 0.5*( m(i)*beta(i)^2 +
m(i+1)*beta(i+1)^2)*dt;

    g2 = g2 + 0.5*( beta(i)*g2d1(i) +
beta(i+1)*g2d1(i+1)...
-beta(i)*g2d2(i) - beta(i+1)*g2d2(i+1))*dt;

    g3 = g3 + 0.5*( beta(i)*g3d1(i)+beta(i)*g3d2(i) +
beta(i+1)*g3d1(i+1)+...
beta(i+1)*g3d2(i+1)+ beta(i)*g3d3(i) +
beta(i+1)*g3d3(i+1))*dt;

    g4 = g4 + 0.5*( beta(i)*g4d2(i) +
beta(i+1)*g4d2(i+1))*dt;

    g5 = g5 + 0.5*( beta(i)*g5d1(i)+0.5*beta(i)*g5d2(i) +
beta(i+1)*g5d1(i+1)+...
0.5*beta(i+1)*g5d2(i+1))*dt;

    g6 = g6 + 0.25*( beta(i)*g6d(i) +
beta(i+1)*g6d(i+1))*dt;

```

```

        end;

        sim simsBio

        v=qout;
end;

t=20;
N=2^t;
Y = fft(v,N);
Pyy =(1000/4)*Y.* conj(Y) / N;
f = (1/tout(2))*(0:(N/2)-1)/N;

figure (1)
plot (tout,v)
xlabel('Time (Milisecond)')
ylabel('v(L,t) (Micrometer)')
title('Time Response')

figure (2)
plot(f,Pyy(1:N/2))
xlabel('Frequency (KHz)')
ylabel('v(L,t) (Micrometer)')
title('Frequency Response')

```


REFERENCES

- [1] Achyuthan K.E., Bergstedt T.S., Chen L., Jones R.M., Kumaraswamy S., Kushon S.A., Ley K.D., Lu L., McBranch D., Mukundan H., Rininsland F., Shi X., Xia W., and Whitten D.G., "Fluorescence Superquenching of Conjugated Polyelectrolytes: Applications for Biosensing and Drug Discovery", *Journal of Materials Chemistry*, **15**, pp. 2648–2656, 2005.
- [2] André P., *Vibration Control of Active Structures: An Introduction*, Kluwer Academic Publishers, Netherlands, 1997, Reprinted 1999.
- [3] Atkinson, A., "Macro- and Microstress Analysis in Sol-gel Derived $\text{Pb}(\text{Zr}_x\text{Ti}_{1-x})\text{O}_3$ Thin Films", *British Ceramic Proceedings*, **54**, pp. 1-7, 1995.
- [4] Barnes J.R., Stephenson R.J., Welland M.E., Gerber Ch., and Gimzewski J.K., "Photothermal Spectroscopy with Femtojoule Sensitivity Using a Micromechanical Device", *Nature*, **372**, pp. 79-81, 1994.
- [5] Barnes J.R., Stephenson R.J., Woodburn C.N., O'Shea S.J., Welland M.E., Rayment T., Gimzewski J.K., and Gerber Ch., "A Femtojoule Calorimeter Using Micromechanical Sensors", *Review of Scientific Instruments*, **65** (12), pp. 3793-3798, 1994.
- [6] Baselt D.R., Lee G.U., and Colton R.J., "Biosensor Based on Force Microscope Technology", *Journal of Vacuum Science & Technology B*, **14** (2), pp. 789-793, 1996.
- [7] Baselt D.R., Lee G.U., Hansen K.M., Chrisey L.A., and Colton R.J., "A High-Sensitivity Micromachined Biosensor", *Proceedings of the IEEE*, **85** (4), pp. 672-680, 1997.
- [8] Beer F.P., and Johnston E.R., *Mechanics of Materials*, McGraw-Hill, New York, 1981.
- [9] Berger R., Delamarche E., Lang H.P., Gerber C., Gimzewski J.K., Meyer E., and Guntherodt H.-J., "Surface Stress in the Self-Assembly of Alkanethiols on Gold", *Science*, **276**, pp. 2021–2023, 1997.

- [10] Berger R., Gerber Ch., and Gimzewski J.K., “Thermal Analysis Using a Micromechanical Calorimeter”, *Applied Physics Letters*, **69** (1), pp. 40- 42, 1996.
- [11] Britton C.L., Jones R.L., Oden P.I., Hu Z., Warmack R.J., Smith S.F., Bryan W.L., and Rochelle J.M., “Multiple-Input Microcantilever Sensors”, *Ultramicroscopy*, **82**, pp. 17-21, 2000.
- [12] Butt H.J., “A Sensitive Method to Measure Changes in the Surface Stress of Solids”, *Journal of Colloid and Interface Science*, **180**, pp. 251–260, 1996.
- [13] Chen G.Y., Thundat T., Wachter E.A., and Warmack R.J., “Adsorption-Induced Surface Stress and Its Effects on Resonance Frequency of Microcantilevers”, *Journal of Applied Physics*, **77** (8), pp. 3618- 3622, 1995.
- [14] Cleveland J.P., Manne S., Bocek D., and Hansma P.K., “A Nondestructive Method for Determining the Spring Constant of Cantilevers for Scanning Force Microscopy”, *Review of Scientific Instruments*, **64** (2), pp. 403-405, 1993.
- [15] Dadfarnia M., Jalili N., Liu Z., and Dawson D.M., “An Observer-based Piezoelectric Control of Flexible Cartesian Robot Arms: Theory and Experiment”, *Control Engineering Practice*, **12**, pp. 1041–1053, 2004.
- [16] Dareing D.W., and Thundat T., “Simulation of Adsorption-Induced Stress of a Microcantilever Sensor”, *Journal of Applied Physics*, **97**, pp. 043526, 2005.
- [17] Datskos P.G., Oden P.I., Thundat T., Wachter E.A., Warmack R.J., and Hunter S.R., “Remote Infrared Radiation Detection Using Piezoresistive Microcantilevers”, *Applied Physics Letters*, **69** (20), pp. 2986- 2988, 1996.
- [18] Esmailzadeh E., and Jalili N., “Parametric Response of Cantilever Timoshenko Beams with Tip Mass under Harmonic Support Motion”, *International Journal of Non-Linear Mechanics*, **33** (5), pp. 765-781, 1998.
- [19] Freund L.B., Floro J.A., and Chason E., “Extensions of the Stoney Formula for Substrate Curvature to Configurations with Thin Substrates or Large Deformations”, *Applied Physics Letters*, **74** (14), pp. 1987-1989, 1999.

- [20] Fritz J., Baller M.K., Lang H.P., Rothuizen H., Vettiger P., Meyer E., Guntherodt H.-J., Gerber Ch., and Gimzewski J.K., “Translating Biomolecular Recognition into Nanomechanics”, *Science*, **288**, pp. 316-318, 2000.
- [21] Gfeller K.Y., Nugaeva N., and Hegner M., “Rapid Biosensor for Detection of Antibiotic-Selective Growth of *Escherichia coli*”, *Applied and Environmental Microbiology*, **71** (5), pp. 2626–2631, 2005.
- [22] Gimzewski J.K., Gerber Ch., Meyer E., and Schlittler R.R., “Observation of a Chemical Reaction Using a Micromechanical Sensor”, *Chemical Physics Letters*, **217**, pp. 589-594, 1994.
- [23] Gunter R.L., Zhine R., Delinger W.G., Manygoats K., Kooser A., and Porter T.L., “Investigation of DNA Sensing Using Piezoresistive Microcantilever Probes”, *IEEE Sensors Journal*, **4** (4), pp. 430- 433, 2004.
- [24] Gupta A., Akin D., and Bashir R., “Detection of Bacterial Cells and Antibodies using Surface Micromachined Thin Silicon Cantilever Resonators”, *Journal of Vacuum Science & Technology B*, **22** (6), pp. 2785-2791, 2004.
- [25] Gupta A., Akin D., and Bashir R., “Single Virus Particle Mass Detection Using Microresonators with Nanoscale Thickness”, *Applied Physics Letters*, **84** (11), pp. 1976-1978, 2004.
- [26] Hansen K.M., Ji H.-F., Wu G., Datar R., Cote R., Majumdar A., and Thundat T., “Cantilever-Based Optical Deflection Assay for Discrimination of DNA Single-Nucleotide Mismatches”, *Analytical Chemistry*, **73** (7), pp. 1567- 1571, 2001.
- [27] Ibach H., “The Role of Surface Stress in Reconstruction, Epitaxial Growth and Stabilization of Mesoscopic Structures”, *Surface Science Reports*, **29**, pp. 193-263, 1997.
- [28] Ilic B., Craighead H.G., Krylov S., Senaratne W., Ober C., and Neuzil P. “Attogram Detection Using Nanoelectromechanical Oscillators”, *Journal of Applied Physics*, **95** (7), pp. 3694- 3703, 2004.
- [29] Ilic B., Yang Y. and Craighead H.G., “Virus detection using nanoelectromechanical devices”, *Applied Physics Letter*, **85** (13), pp. 2604-2606, 2004.

- [30] Jensenius H., Thaysen J., Rasmussen A.A., Veje L.H., Hansen O., and Boisen A., "Microcantilever-based Alcohol Vapor Sensor-application and Response Model", *Applied Physics Letters*, **76** (18), pp. 2615-2617, 2000.
- [31] Kirstein K.-U., Li Y., Zimmermann M., Vancura C., Volden T., Song W.H., Lichtenberg J., and Hierlemann A., "Cantilever-based Biosensors in CMOS Technology", *Proceedings of the Design, Automation and Test in Europe Conference and Exhibition (DATE'05)*, pp. 1340-1341, 2005.
- [32] Klein, C.A., "How Accurate Are Stoney's Equation and Recent Modifications", *Journal of Applied Physics*, **88** (9), pp. 5487- 5489, 2000.
- [33] Klein C.A., and Miller R., "Strains and Stresses in Multilayered Elastic Structures: The Case of Chemically Vapor-Deposited ZnS/ZnSe Laminates", *Journal of Applied Physics*, **87**, pp. 2265-2272, 2000.
- [34] Koch R., and Abermann R., "On the Influence of Thermal Effects on Internal Stress Measurements during and After Deposition of Silver, Gold and Copper Films", *Thin Solid Films*, **129**, PP. 63-70, 1985.
- [35] Lai L., Perazzo T., Shi Z., and Majumdar A., "Optimization and Performance of High-resolution Micro-optomechanical Thermal Sensor", *Sensors and Actuators A*, **58**, pp. 113-119, 1997.
- [36] Lang H.P., Berger R., Battiston F., Ramseyer J.-P., Meyer E., Andreoli C., Brugger J., Vettiger P., Despont M., Mezzacasa T., Scandella L., Güntherodt H.-J., Gerber Ch., and Gimzewski J.K., "A Chemical Sensor Based on a Micromechanical Cantilever Array for the Identification of Gases and Vapors", *Applied Physics A*, **66** (7), pp. S61-S64, 1998.
- [37] Lavrik N.V., Sepaniak M.J., and Datskos P.G., "Cantilever Transducers as a Platform for Chemical and Biological Sensors", *Review of Scientific Instruments*, **75** (7), pp. 2229- 2253, 2004.
- [38] Lee J.H., Kim T.S., and Yoon K.H., "Effect of mass and stress on resonant frequency shift of functionalized $\text{Pb}(\text{Zr}_{0.52}\text{Ti}_{0.48})\text{O}_3$ thin film microcantilever for the detection of C-reactive protein", *Applied Physics Letter*, **84** (16), pp. 3187-3189, 2004.
- [39] Lu P., Shen F., O'Shea S.J., Lee K.H., and Ng T.Y., "Analysis of Surface Effects on Mechanical Properties of Microcantilevers", *Materials Physics and Mechanics*, **4**, pp. 51–55, 2001.

- [40] Mahmoodi S.N., Khadem S.E., and Jalili N., “Theoretical Development and Closed-form Solution of Nonlinear Vibrations of a Directly Excited Nanotube-reinforced Composite Cantilevered Beam”, *Archive of Applied Mechanics*, **75**, pp. 153–163, 2006.
- [41] Martinez R.E., Augustyniak W.M., and Golovchenko J.A., “Direct Measurement of Crystal Surface Stress”, *Physical Review Letters*, **64** (9), pp. 1035-1038, 1990.
- [42] McFarland A., Poggi M., Doyle M., Bottomley L., and Colton J., “Influence of Surface Stress on the Resonance Behavior of Microcantilevers”, *Applied Physics Letters*, **87**, pp. 053505, 2005.
- [43] Miyatani T., and Fujihira M., “Calibration of Surface Stress Measurements with Atomic Force Microscopy”, *Journal of Applied Physics*, **81** (11), pp. 7099-7115, 1997.
- [44] Oden P.I., “Gravimetric Sensing of Metallic Deposits Using an End-loaded Microfabricated Beam Structure”, *Sensors and Actuators B*, **53**, pp. 191–196, 1998.
- [45] Oden P.I., Chen G.Y. , Steele R.A., Warmack R.J., and Thundat T., “Viscous Drag Measurements Utilizing Microfabricated Cantilevers”, *Applied Physics Letters*, **68** (26), pp. 3814- 3816, 1999.
- [46] Oden P.I., Datskos P.G., Thundat T., and Warmack R.J., “Uncooled Thermal Imaging Using a Piezoresistive Microcantilever”, *Applied Physics Letters*, **69** (21), pp. 3277-3279, 1996.
- [47] Patel S.S., and Tirrel M., “Measurement of Forces between Surfaces in Polymer Fluids”, *Annual Review of Physical Chemistry*, **40**, pp. 597–635, 1989.
- [48] Perazzo T., Mao M., Kwon O., Majumdar A., Varesi J.B, and Norton P., “Infrared Vision Using Uncooled Micro-optomechanical Camera”, *Applied Physics Letters*, **74** (23), pp. 3567- 3569, 1999.
- [49] Raiteri R., and Butt H.-J., “Measuring Electrochemically Induced Surface Stress with an Atomic Force Microscope”, *Journal of Physical Chemistry*, **99**, pp. 15728-15732, 1995.

- [50] Ren Q., and Zhao Y.-P., “Influence of Surface Stress on Frequency of Microcantilever-based Biosensors”, *Microsystem Technologies*, **10**, pp. 307-314, 2004.
- [51] Sader J.E., “Surface Stress Induced Deflections of Cantilever Plates with Applications to the Atomic Force Microscope: Rectangular Plates”, *Journal of Applied Physics*, **89** (5), pp. 2911-2921, 2001.
- [52] Sader J.E., Larson I., Mulvaney P., and White L.R., “Method for the Calibration of Atomic Force Microscope Cantilevers”, *Review of Scientific Instruments*, **66** (7), pp. 3789-3798, 1995.
- [53] Savran C.A., Knudsen S.M., Ellington A.D., and Manalis S.R., “Micromechanical Detection of Proteins Using Aptamer-Based Receptor Molecules”, *Analytical Chemistry*, **76**, pp. 3194-3198, 2004.
- [54] Schell-Sorokin A.J., and Tromp, R.M., “Mechanical Stress in (Sub)-monolayer Epitaxial Films”, *Physical Review Letters*, **64** (9), pp. 1039, 1990.
- [55] Sepaniak M., Datskos P., Lavrik N., and Tipple C., “Microcantilever Transducers: A New Approach in Sensor Technology”, *Analytical Chemistry*, **74** (21), pp. 568 A-575 A, 2002.
- [56] Shuttleworth R., “The Surface Tension of Solids”, *Proceedings of the Physical Society*, **63** (5), pp. 444-457, 1950.
- [57] Sitti M., and Hashimoto H., “Controlled Pushing of Nanoparticles: Modeling and Experiments”, *IEEE/ASME Transactions on Mechatronics*, **5** (2), pp. 199-211, 2000.
- [58] Stokes R.J., and Evans D.F., *Fundamentals of Interfacial Engineering*, Wiley–VCH, New York, 1997.
- [59] Stoney G.G., “The tension of Metallic Films Deposited by Electrolysis”, *Proceedings of the Royal Society of London A*, **82**, pp. 172-175, 1909.
- [60] Su M., Li S., and Dravid V.P., “Microcantilever Resonance-based DNA Detection with Nanoparticle Probes”, *Applied Physics Letter*, **82** (20), pp. 3562- 3564, 2003.

- [61] Subramanian A., Oden P.I., Kennel S.J., Jacobson K.B., Warmack R.J., Thundat T., and Doktycz M.J., "Glucose Biosensing using an Enzyme-coated Microcantilever", *Applied Physics Letter*, **81** (2), pp. 385- 387, 2002.
- [62] Taylor E.H., and Waggener W.C., "Measurement of Adsorptive Forces", *Journal of Physical Chemistry*, **83** (10), pp. 1361-1362, 1979.
- [63] Thundat T., Chen G.Y., Warmack R.J., Allison D.P., and Wachter E.A. "Vapor Detection Using Resonating Microcantilevers", *Analytical Chemistry*, **67**, pp. 519-521, 1995.
- [64] Thundat T., Oden P.I., and Warmack R.J., "Microcantilever Sensors", *Microscale Thermophysical Engineering*, **1**, pp. 185-199, 1997.
- [65] Thundat T., Wachter E.A., Sharp S.L., and Warmack R.J., "Detection of Mercury Vapor Using Resonating Microcantilevers", *Applied Physics Letters*, **66** (13), pp. 1695- 1697, 1995.
- [66] Thundat T., Warmack R.J., Chen G.Y., and Allison D.P., "Thermal and Ambient-induced Deflections of Scanning Force Microscope Cantilevers", *Applied Physics Letters*, **64** (21), pp. 2894- 2898, 1994.
- [67] Townsend P.H., Barnett D.M., and Brunner T.A., "Elastic Relationship in Layered Composite Media with Approximation for the Case of Thin Films on a Thick Substrate", *Journal of Applied Physics*, **62** (11), pp. 4438-4444, 1987.
- [68] Wachter E.A., and Thundat T., "Micromechanical Sensors for Chemical and Physical Measurements", *Review of Scientific Instruments*, **66** (6), pp. 3662- 3667, 1995.
- [69] Wachter E.A., Thundat T., Oden P.I., Warmack R.J., Datskos P.G., and Sharp S.L., "Remote Optical Detection Using Microcantilevers", *Review of Scientific Instruments*, **67** (10), pp. 3434- 3439, 1996.
- [70] Weigert S., Dreier M., and Hegner M., "Frequency Shifts of Cantilevers Vibrating in Various Media", *Applied Physics Letters*, **69** (19), pp. 2834- 2836, 1996.
- [71] Wu G., Ji H., Hansen K., Thundat T., Datar R., Cote R., Hagan M.F., Chakraborty A.K., and Majumdar A., "Origin of Nanomechanical Cantilever Motion Generated from Biomolecular Interactions", *Proceedings of the National Academy of Sciences*, **98** (4), pp. 1560–1564, 2001.

- [72] Yu N., and Polycarpou A.A., “Adhesive Contact Based on the Lennard–Jones Potential: A Correction to the Value of the Equilibrium Distance as Used in the Potential”, *Journal of Colloid and Interface Science*, **278**, pp. 428–435, 2004.
- [73] Zhang W., and Turner K., “Frequency-Tuning for Control of Parametrically Resonant Mass Sensors”, *Journal of Vacuum Science and Technology A*, **23** (4), pp. 841-845, 2005.
- [74] Zhang Y., Ren Q., and Zhao Y., “Modeling Analysis of Surface Stress on a Rectangular Cantilever Beam”, *Journal of Physics D: Applied Physics*, **37**, pp. 2140–2145, 2004.
- [75] Zhou X.C., O’Shea S.J., and Sam Fong Yau Li, “Amplified Microgravimetric Gene Sensor using Au Nanoparticle Modified Oligonucleotides”, *Chemical Communications*, pp. 953–954, 2000.
- [76] <http://www.pharmaceutical-int.com/categories/qcm-technology/quartz-crystal-microbalance-qcm.asp>
- [77] <http://www.q-sense.com>
- [78] <http://www.masscal.com/instrument.html>